ARTICLE

ER-to-Golgi trafficking of procollagen in the absence of large carriers

Janine McCaughey[1] , Nicola L. Stevenson[1] , Stephen Cross[2], and David J. Stephens[1]

Secrecion and assembly of collagen are fundamental to the function of the extracellular matrix. Defects in the assembly of a collagen matrix lead to pathologies including fibrosis and osteogenesis imperfecta. Owing to the size of fibril-forming procollagen molecules it is assumed that they are transported from the endoplasmic reticulum to the Golgi in specialized large COPII-dependent carriers. Here, analyzing endogenous procollagen and a new engineered GFP-tagged form, we show that transport to the Golgi occurs in the absence of large (>350 nm) carriers. Large GFP-positive structures were observed occasionally, but these were nondynamic, are not COPII positive, and are labeled with markers of the ER. We propose a short-loop model of COPII-dependent ER-to-Golgi traffic that, while consistent with models of ERGIC-dependent expansion of COPII carriers, does not invoke long-range trafficking of large vesicular structures. Our findings provide an important insight into the process of procollagen trafficking and reveal a short-loop pathway from the ER to the Golgi, without the use of large carriers.

Introduction

Collagen is the most abundant protein in the body. Fibrillar type I collagen plays a key role in bone, skin, and tendon formation, providing tissues with the necessary structural support. Altered collagen secretion, processing, and assembly are linked to diseases including osteogenesis imperfecta, fibrosis, chondrodysplasia, Ehlers–Danlos syndrome, and many more (Jobling et al., 2014; Forlino and Marini, 2016). Type I collagen assembles from two type I α1 chains together with one type I α2 chain to form trimeric procollagen in the ER (Goldberg et al., 1972; Canty and Kadler, 2005), with the α-helix from each chain forming a rigid 300-nm triple helix structure (Bächinger et al., 1982; Lightfoot et al., 1992). During procollagen biosynthesis, proline hydroxylation stabilizes the triple helical conformation (Jimenez et al., 1973; Blanck and Peterkofsky, 1975). This process requires the presence of ascorbic acid, which acts as a cofactor for prolyl-4-hydroxylase (Mussini et al., 1967). The collagen-specific chaperone heat shock protein 47 (Hsp47; Satoh et al., 1996; Ito and Nagata, 2017) is also required.

To be secreted efficiently, procollagen I must traffic from the ER to the Golgi via the ER–Golgi intermediate compartment (ERGIC; Satoh et al., 1996; Malhotra and Erlmann, 2015; Malhotra et al., 2015). Conventional ER-to-Golgi transport is facilitated by coat protein complex type II (COPII) vesicles with a size of 60–90 nm in diameter. These vesicles are thus significantly smaller than the

300-nm length of procollagen. Nonetheless, COPII vesicles are essential for efficient collagen trafficking in cells (Stephens and Pepperkok, 2002; Townley et al., 2008, 2012) and in animal models since perturbation of, or mutations in, key COPII components including Sec24D (Sarmah et al., 2010; Garbes et al., 2015; Moosa et al., 2016), Sec23A (Boyadjiev et al., 2006; Lang et al., 2006), and Sec13 (Townley et al., 2008, 2012; Schmidt et al., 2013), cause defects in collagen secretion. To accommodate all of these data the prevailing hypothesis for the mechanism of procollagen secretion proposes the formation of large COPII carriers (Saito et al., 2009; Venditti et al., 2012; Nogueira et al., 2014; Malhotra and Erlmann, 2015; Saito and Katada, 2015; Santos et al., 2015; McGourty et al., 2016; Gorur et al., 2017), some in the range of 400–1,200 nm and often seen to be >1 μm. Formation of these carriers is said to be facilitated by the ER transmembrane proteins transport and Golgi organization 1 (TANGO1, also called Mia3) and cTAGE5 (a TANGO1-related protein) that form a dimer and localize to ER exit sites (ERES) in mammals (Saito et al., 2011). TANGO1 is considered to act as a tether to the ERGIC to expand the nascent procollagen-containing carrier during its formation.

Several publications have shown large structures reported to be ER-to-Golgi carriers of procollagen (Jin et al., 2012; McGourty et al., 2016; Gorur et al., 2017). These large structures are generally few in number and seen in systems where the ubiquitin ligase

---

[1]Cell Biology Laboratories, School of Biochemistry, Faculty of Life Sciences, University of Bristol, Bristol, UK;   [2]Wolfson Bioimaging Facility, Faculty of Biomedical Sciences, University of Bristol, Bristol, UK.

Correspondence to David J. Stephens: david.stephens@bristol.ac.uk.

Cullin3 (CUL3) adaptor Kelch-like protein 12 (KLHL12) is overexpressed (Jin et al., 2012). CUL3 facilitates monoubiquitylation of Sec31, stalling the outer complex formation, leading to a delayed scission and enlargement of COPII vesicles (Jin et al., 2012). Subsequent work defined a mechanism for KLHL12-mediated ubiquitylation of Sec31A, with PEF1 and ALG2 shown to be subunits of the CUL3-KLHL12 ubiquitin ligase (McGourty et al., 2016). Consistent with the previous finding, the large structures labeled for Sec31A, PEF1, and ALG-2 and, more significantly, with antibodies against procollagen (McGourty et al., 2016). Similar large, procollagen- and Sec31A-positive structures have been shown in KI6 cells that overexpress both type I procollagen and FLAG-KLHL12 (Gorur et al., 2017). Apparent encapsulation of procollagen into large (∼800-nm) Sec31A structures was shown by correlative light EM (Gorur et al., 2017). Smaller Sec31A puncta remained devoid of procollagen labeling. Short-range movement of these carriers, using live-cell imaging of procollagen-GFP, did not appear to be Golgi-directed and occurred over distances of only a few micrometers. Further support for this model came from experiments showing COPII-dependent packaging of procollagen in vitro into large structures (Gorur et al., 2017; Yuan et al., 2017).

Pathways for transport of procollagen from the ER to the Golgi have to date relied extensively on a COL1A1-GFP construct with a C-terminal GFP tag (Stephens and Pepperkok, 2002). Expression of this construct reveals the presence of small ascorbate-dependent, highly mobile long-range transport carriers containing procollagen-GFP. While generally effective, there are caveats to its use. Many cells do not traffic this fusion protein effectively. This compromised ability to assemble and traffic is most likely because the folding of the procollagen trimer proceeds from the C terminus (Kadler et al., 1990; Bourhis et al., 2012).

Our aim was to test the prevailing hypothesis that large vesicular carriers mediate procollagen secretion. To achieve this, we generated a newly designed procollagen construct incorporating some key features to better control and define secretory cargo export from the ER. Surprisingly, live-cell imaging using this construct revealed that procollagen traffics from the ER to the Golgi without using large vesicular carriers. Instead the Golgi gradually fills with procollagen upon ascorbate addition, while the ER empties, suggesting the existence of a short trafficking loop connecting the ER and Golgi. Combined with work on endogenous procollagen and a variety of cell types, we propose a new mode of procollagen trafficking via a short-loop pathway that facilitates local transfer of procollagen from the juxtanuclear ER to the Golgi.

Results

An ascorbate- and biotin-controllable procollagen reporter: SBP-mGFP-COL1a1

To visualize ER-to-Golgi trafficking of procollagen for study, we engineered monomeric GFP (mGFP) and a streptavidin-binding peptide (SBP) tag into procollagen 1α1. The tag was introduced upstream of the naturally occurring N-terminal proteolytic cleavage site (located after the N-terminal propeptide) to generate SBP-mGFP-COL1a1 (abbreviated here to GFP–COL; Fig. 1 A). The inclusion of the SBP tag allows synchronization of traffick-

ing using the Retention Using Selective Hooks (RUSH) system to control cargo exit from the ER using biotin (Boncompain et al., 2012). When expressed transiently in IMR-90 human lung fibroblasts (Fig. 1 B, i) and in human telomerase immortalized retinal pigment epithelial cells (hTERT-RPE-1; Fig. 1 B, ii), GFP–COL colocalizes with Hsp47 in the ER but not with the cis-Golgi marker GM130 at steady state (Fig. 1 C, i). Following the addition of ascorbate, GFP–COL became enriched in the Golgi area (Fig. 1 C, ii and iii).

As expected, transient transfection of GFP–COL–positive cells led to highly variable expression levels. To reduce the variability an RPE-1 cell line was created that stably expresses GFP–COL (GFP–COL–RPE). The population was sorted into four equally distributed populations, with different expression levels according to signal intensity of GFP, and the 25% of cells expressing the lowest level were chosen for future experiments. For further analysis of transport to the Golgi, GFP–COL–RPE cells were cotransfected with a bicistronic construct encoding an ER hook (KDEL-tagged streptavidin to retain the SBP fusion protein in the ER) and a separate trans-Golgi marker that expressed the minimal Golgi targeting region of sialyltransferase fused to mCherry (ST-Cherry). The coexpression of the ER hook here enabled the retention of SBP-tagged GFP–COL in the ER lumen until addition of biotin to trigger the dissociation of SBP from the streptavidin-bound KDEL hook.

Live-cell imaging of synchronized procollagen transport using confocal microscopy was then used to monitor the dynamics of ER-to-Golgi transport. Prior to addition of ascorbate and biotin (asc/biotin), GFP–COL and the Golgi marker show no significant colocalization (Fig. 1 D, t = 0). After addition of asc/biotin, GFP–COL structures of high signal intensity appeared near the Golgi, as well as in the cell periphery (Fig. 1 D, t = 15; and Video 1). The signal intensity of GFP–COL in the ER decreased gradually over time, while the accumulation of GFP–COL in and around the trans-Golgi further increased (Video 1). After filling of the Golgi an overall decrease of GFP–COL signal intensity occurred over time. Line scans in Fig. 1 D show clearly this accumulation of GFP–COL around the ST-Cherry–labeled Golgi compartments (t = 16 min), before GFP–COL fills the trans-Golgi (here, at 24 min asc/biotin) and subsequently exits (t = 40 and 51 min in this example). These experiments are consistent with ascorbate-dependent transport of GFP–COL to the Golgi, followed by its secretion from the cell. Fig. S1 A (derived from Video 2) shows that the addition of ascorbate alone is insufficient to release GFP–COL when coexpressed with a hook (in this case a KDEL-tagged streptavidin as ER hook and separate cis-Golgi marker mannosidase II tagged with mScarlet-i, a red fluorescent protein (Bindels et al., 2017; MannII-mSc). Fig. S1 shows ascorbate- and biotin-dependent trafficking in hTERT-BJ5Ta human fibroblasts (Fig. S1 B and Video 3). Ascorbate-dependent trafficking in IMR-90 human fibroblasts is shown in Fig. S1 C and Video 4.

Surprisingly, in the above experiments we failed to observe the formation of any large, dynamic carriers before procollagen reaching the Golgi. Imaging at a higher frame rate (Fig. S2 and Video 5) also failed to reveal any large puncta that translocate toward the Golgi. In some experiments (more noticeably in transiently transfected cells) we did detect a very small number
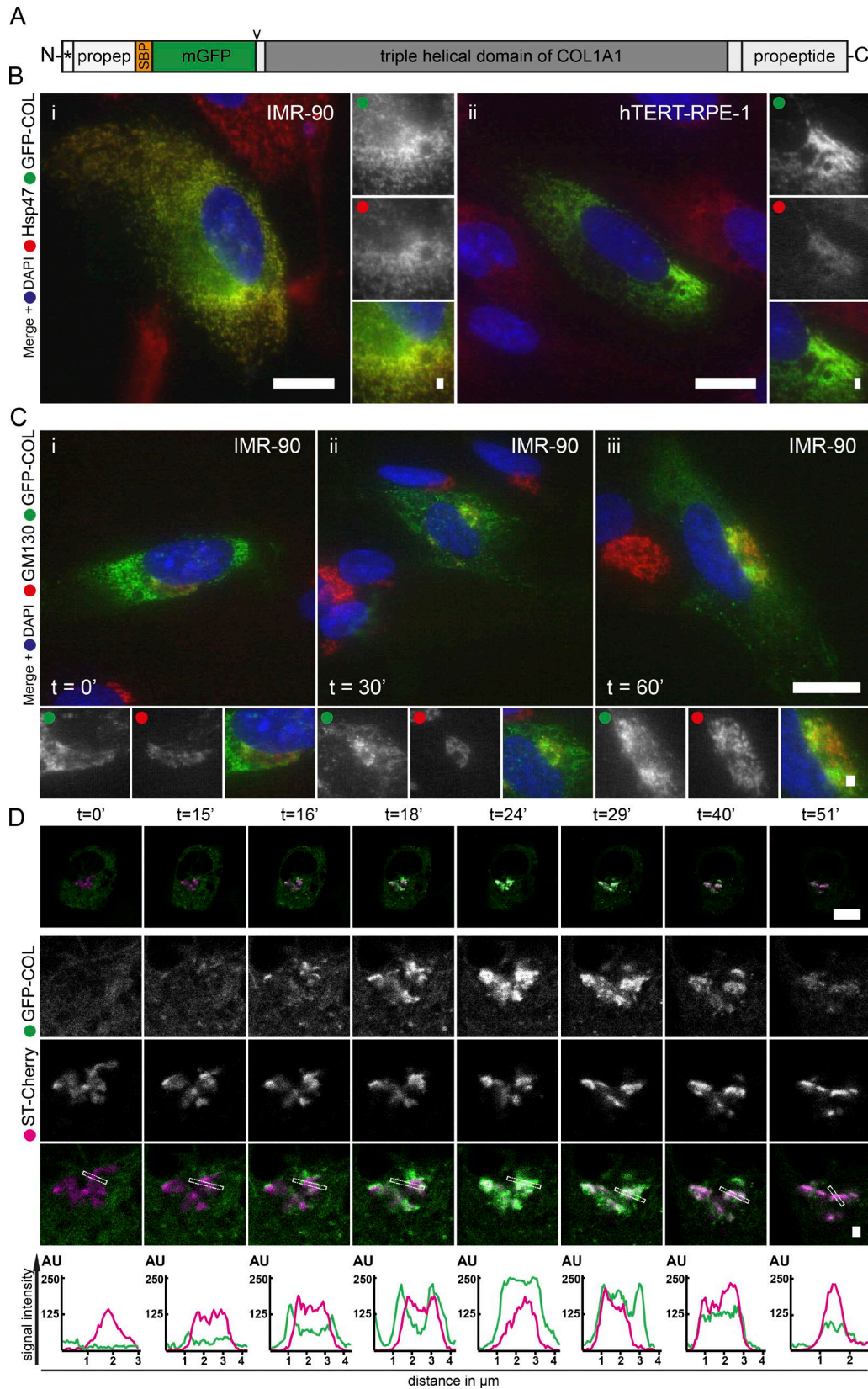
Figure 1. **Controllable ER-to-Golgi trafficking of GFP–COL in the absence of large carriers. (A)** The GFP–COL fusion construct. It consists of a synthetic prosequence of human COL1A1 followed by an SBP, mGFP, the N-propeptide cleavage site (indicated by the arrowhead) within the nonhelical region, and the triple-helical domain with the C-terminal nonhelical region followed by the C-propeptide of human COL1A1. The signal sequence is indicated by the asterisk. **(B and C)** Widefield microscopy of cells transiently expressing GFP–COL (A). 16 h after transfection, GFP-COL (green) colocalized with Hsp47 (red) in the ER in IMR-90 (B, image i) and RPE-1 (B, image ii) cells. Large images show whole cells, while the small panels show the enlargements with the corresponding

McCaughey et al.
ER-to-Golgi traffic of procollagen

Journal of Cell Biology
https://doi.org/10.1083/jcb.201806035

931

(typically one per cell) of punctate structures that translocate to the Golgi along curvilinear tracks, consistent with previously described vesicular tubular structures (Stephens and Pepperkok, 2002). An example of this is Fig. S1 B and Video 3, where a GFP-positive structure with a maximum estimated size of 535 nm translocates to the Golgi over the nucleus at ∼17 min after asc/biotin. Similarly, Fig. S2 and Video 5 show one such structure tracking toward the Golgi over the nucleus (highlighted by arrowheads from 10′03″ to 11′00″). Collectively, these data suggest ER-to-Golgi transport in the absence of large carriers. We therefore sought to define this in more detail.

ER-to-Golgi trafficking of GFP–COL occurs without the use of large carriers

In ∼50% of all live cells, we did observe between one and four large, round GFP–COL structures (calculated diameter, >1 µm) that were similar in appearance to those previously reported. For example, Fig. 2, A and B, shows GFP–COL distributed throughout the ER and in four larger (1–2-µm diameter), circular, GFP-positive structures with elevated signal intensity compared with the ER background (Fig. 2 B, circles). However, these structures were relatively static and did not change in size or intensity despite transport of GFP–COL to the Golgi (Fig. 2, A–D; and Videos 6 and 7). They also did not appear to be the source or destination of the few more dynamic punctate structures observed (e.g., highlighted by arrows in Fig. 2 A). In one example, a larger (∼1.4-µm diameter) circular structure was observed moving over ∼2 µm, while maintaining its size and the same slightly higher signal compared with the GFP–COL signal from the surrounding ER (Fig. 2 C, circle; and Video 7), but this structure did not interact with the Golgi. As seen in Fig. 2, C and D, again no notable vesicular transport toward the Golgi can be detected from the time point of accumulation around the Golgi to the end of the measurement after 26 min asc/biotin in this cell (Video 7). Extensive analysis of GFP–COL–RPE also failed to reveal any significant GFP-positive large carriers contributing to the accumulation of GFP–COL in the Golgi. The earliest stages of accumulation of GFP–COL proximal to the Golgi suggest an accumulation of GFP–COL at the ER–Golgi interface (e.g., Fig. 2 D and Video 7, t = 9′30″–11′00″), before entering the Golgi.

Large GFP–COL structures are positive for ER and Hsp47, not COPII

To further define the nature of the large immobile GFP-positive structures, cells were fixed during live-cell imaging experiments at time points when an accumulation of GFP–COL in or around the Golgi was observed (Videos 6 and 8). Fig. 3 A shows labeling for the endogenous cis/medial-Golgi marker giantin and ST-Cherry in these cells; the separation between markers is consistent with the expected localization of ST-Cherry as a trans-Golgi marker. We found that the large GFP-positive structures observed were negative for giantin (Fig. 3 A, ii, circle); however, they did colocalize with the collagen-specific chaperone Hsp47 (Fig. 3 B, i, circle). Therefore, these structures are not bona fide Golgi elements. To determine whether these large Hsp47-positive structures were part of the ER or post-ER structures, we used an ER membrane marker, Cyt-ERM-mScarlet-i. This construct encodes mScarlet-i fused to the ER-targeting sequence of cytochrome P450 (Costantini et al., 2012). The large GFP–COL structures colocalized with both Hsp47 and ezrin, radixin, and moesin (ERM; Fig. 3 C, i and ii, circles).

To investigate whether any of these structures were COPII carriers, cells were colabeled for the COPII marker Sec31A (Fig. 3 D). We analyzed the size distribution of GFP-positive structures relative to their overlap with Sec31A (Fig. 3 E). Large GFP–COL structures (>1-µm diameter) were found in approximately one fifth of the cells analyzed, but these did not show any colocalization with Sec31A (Fig. 3, D [i, circle] and E), nor did 95% of small GFP-positive structures (<350-nm diameter; example shown in Fig. 3 D, i and ii, arrows). Any GFP-positive puncta that did show a higher percentage of overlap with Sec31A (example shown in Fig. 3 D, i and ii, arrowheads) were consistently smaller than those that were negative for Sec31A (Fig. 3 E). Furthermore, the small GFP-positive puncta were negative for both ERM (Fig. 3 C, i and ii, arrow and square) and Golgi markers (Fig. 3 A, i and ii, arrows). While most small punctate GFP-positive structures were also negative for Hsp47 (Fig. 3, B [i and ii] and C [i, arrows]), some were found to indeed colocalize with Hsp47 but not ERM (Fig. 3 C, ii, square).

In all cases, as shown in Figs. 2 D and 3 A, cells show a gradual accumulation of GFP–COL around the rim of the Golgi followed by subsequent filling as described above for Fig. 1 D, without the appearance of significant numbers of peripheral carriers of any size directed toward the Golgi. The only structures positive for both GFP–COL and COPII were small and did not stand out in size compared with other COPII puncta (it should be noted that with confocal imaging and the measuring approach used, objects with a diameter ≤160 nm cannot be differentiated in size). We also found that these larger structures do not label for markers of

---

channels in gray scale and the merged image including nuclear DAPI staining (blue). **(C)** Same image setup as in B with GFP–COL (green) and cis-Golgi marker GM130 (red) labeling in transiently GFP–COL-expressing IMR-90 cells. Time points indicate length of incubation in the presence of 50 µg·ml⁻¹ ascorbate before fixation. A concentration of GFP–COL in the Golgi can be observed after both 30 (C, image ii) and 60 min (C, image iii) in the presence of ascorbate. Number of cells imaged n ≥ 10. **(D)** Confocal images from live-cell imaging of RPE-1 cells stably expressing GFP–COL (green; GFP–COL–RPE) cotransfected with the trans-Golgi marker ST-Cherry (magenta; using the RUSH system). Acquisition at one frame every 30 s. Image layout as in C, followed by line graphs showing the signal intensity (y axis) in arbitrary units for GFP–COL (green) and ST-Cherry (magenta) for the corresponding line with a 5-pixel width drawn through the Golgi in the enlarged overlays. The x axis shows the distance in micrometers. Image stills are derived from Video 1. Time points indicate minutes of incubation in presence of 500 µg·ml⁻¹ ascorbate and 400 µM biotin (asc/biotin). At time point 0 (t = 0 min), GFP–COL and ST-Cherry show distinct localization. Over time an accumulation of GFP–COL around the Golgi marker occurs and increases until t = 18 min, with subsequent filling of the trans-Golgi (t = 24 min). Later time points show the decrease in intensity of GFP–COL overall and in the Golgi area (t = 29, 40, and 51 min), implying functional transport to the Golgi, followed by secretion from the cell. For each set of live imaging experiments, three cells from the same dish were imaged simultaneously. A total of n = 4 sets was acquired. Scale bars, 10 µm; in enlargements, 1 µm.
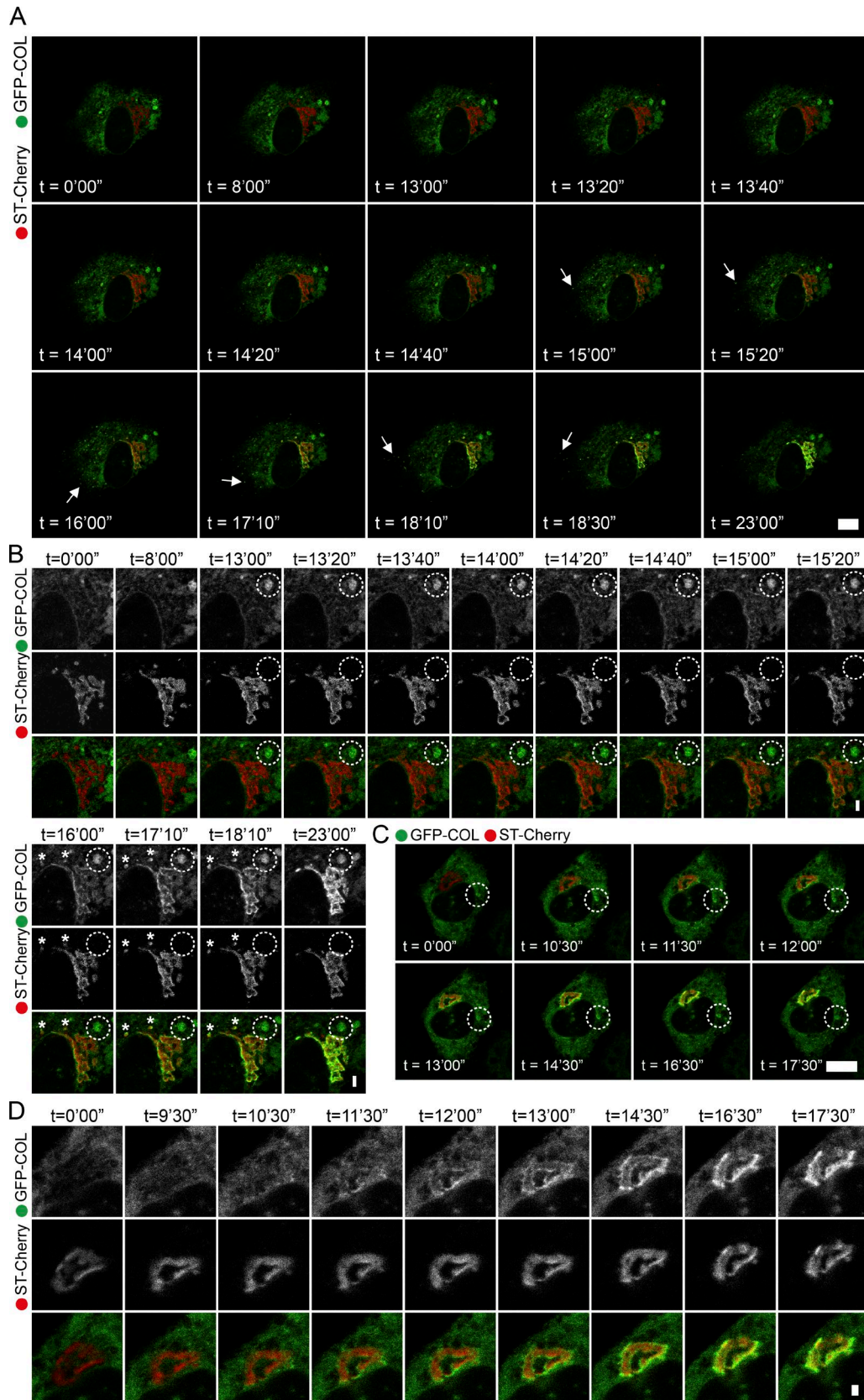

Figure 2. Transport of GFP–COL to the Golgi occurs without the use of large carriers. Image stills from confocal live-cell imaging of RPE-1 cells stably expressing GFP–COL (green; GFP–COL–RPE) cotransfected with the trans-Golgi marker ST-Cherry (red). Time points indicate minutes after addition of asc/biotin. **(A)** A whole cell imaged at one frame every 20 s (derived from Video 6). Probable post-Golgi structures are indicated by arrows. **(B)** Corresponding enlargements of A shown with channels for GFP–COL and ST-Cherry in gray scale, as well as the overlay image. Large circular GFP–COL-positive structures

autophagosomes (Cherry-LC3B, ATG16L, and WIPI2; Fig. S3, A–C, circles) or endosomal markers (EEA1, Rab11, or the transferrin receptor; Fig. S3, D–F, circles).

We observed GFP–COL emerging from Str-KDEL-IRES-mScarlet-i-Sec23A (mSc-Sec23A)–positive ERES (Fig. 4 A, enlarged in Fig. 4 B and Video 9). The filling of adjacent Golgi elements from proximal ERES is apparent in the enlargements shown in Fig. 4 B (arrowheads). We also saw concentration of GFP–COL in peripheral ERES, but it did not result in budding of clearly defined structures. We consider it most likely that small carriers bud from these sites that are not detected in our experiments, owing to a combination of low intensity and being masked by the signal from the ER. We further validated the COPII dependence of this process using a mutant of Sar1 (Sar1-H79G), which prevents GTP hydrolysis and so inhibits the COPII reaction. Expression of Sar1-H79G blocks GFP–COL in the ER even in the presence of ascorbate and biotin (Fig. 4 C).

To provide better resolution, we used gated stimulated emission depletion microscopy (gSTED) to resolve GFP–COL- and COPII-positive structures. Fig. 5 A (enlargement in Fig. 5 B) shows GFP–COL–RPE labeled with both mSc-Sec23A and antibodies against endogenous Sec24C and GFP to maximize detection of the inner layer of the COPII coat and of GFP–COL, respectively. We observed GFP–COL-positive structures ranging from <100 nm to >1 µm and quantified the diameter of these objects by fitting the corresponding line graphs (where possible) to a Gaussian function and measuring the full width at half-maximum (FWHM) intensity. The enlargements, and associated quantification using line scans (Fig. 5 C), show clearly that the largest COPII-positive GFP–COL structures (e.g., Fig. 5 C, i, vii, and x) are not uniformly COPII positive; occasionally, they are associated with small COPII puncta, but these are not consistent with encapsulation and instead are more consistent with clusters of ERES as we have previously described (McCaughey et al., 2016). Where GFP–COL-positive and COPII-positive structures are seen (e.g., Fig. 5 C, ii–v and ix), they are typically <350 nm. Furthermore, large circular GFP-positive structures with diameters >1 µm remain negative for COPII labeling with mSec23A/Sec24C (Fig. 5 C, vi and viii). Therefore, we sought to examine the transport and occurrence of large carriers of endogenous procollagen in fibroblasts secreting large quantities of type I procollagen.

Primary fibroblasts are devoid of large procollagen structures
Immunofluorescence of endogenous procollagen 1α1 in adult primary skin fibroblasts (NHDF-Ad) showed that it colocalizes with the collagen specific chaperone Hsp47 in the ER (Fig. 6 A, i and iv). We also observed partial localization to areas of the Golgi apparatus (Fig. 6 A, ii and iii, arrows), especially at the rim of the Golgi. This appearance is very similar to prior observations made using GFP–COL-expressing cells (most evident in Fig. 1, C [iii] and

D (t = 40), and Fig. 3, A [i and ii] and B [i and ii]). However, in primary fibroblasts, this observation is independent of ascorbate since colocalization with Golgi markers was observed before, as well as after, 30 min of incubation with ascorbate. It is possible that sufficient ascorbate was present in the growth medium to facilitate some proline hydroxylation and procollagen export. Most procollagen-positive punctate structures were negative for the COPII marker Sec31A (Fig. 6 B, i–iv, arrows). Similarly, analysis of nontransformed, telomerase immortalized, human fibroblasts (BJ-5ta) showed procollagen accumulated in the Golgi area in both the presence and absence of ascorbate (Fig. 6 C, i–iv). Some small procollagen puncta were evident, but again these did not colocalize with Sec31A (Fig. 6 C, i–iv, arrows). It was, however, notable that no large structures labeled for either endogenous procollagen 1α1 or Sec31A were detected in these fixed samples in either cell line. Therefore, our data support a direct route of transport from the juxtanuclear ER to the Golgi without the use of large carriers for both endogenous and overexpressed type I procollagen.

We also tested a variety of other anti-COL1A1 antibodies for immunofluorescence with NHDF-Ad and IMR-90 cells (Fig. S4). None of these cells show any large COPII (Sec24C or Sec24D) and/or COL1A1 structures, even when labeling with the same mouse monoclonal antibody previously shown to visualize large COL1A1 structures by other laboratories (Gorur et al., 2017).

GFP–COL transport to the Golgi is not dependent on an intact microtubule network
The absence of long-range carriers translocating from the cell periphery to the Golgi during live-cell imaging led us to question the role of peripheral ERES in procollagen transport. Long-range ER-to-Golgi transport in mammalian systems occurs by translocation along microtubules. Microtubules are not essential for trafficking but optimize the efficiency of transfer between organelles. An intact microtubule network is, however, required to maintain the juxtanuclear organization of the Golgi ribbon. Upon microtubule disassembly, such as in the presence of the drug nocodazole (NZ), the Golgi scatters into functional ministacks dispersed throughout the cytosol adjacent to ERES. NZ can thus be used to disrupt long-range trafficking from peripheral ERES without affecting local ER–Golgi transport at the sites of the ministacks.

To determine the requirement for microtubules, and a juxtanuclear Golgi, in the transport of procollagen, cells were treated with NZ for 60–120 min before imaging. Efficacy of NZ was validated using tubulin labeling (Fig. S5 A). Fig. 7 shows images of GFP–COL–RPE cells 60 min after the addition of NZ followed by addition of asc/biotin/NZ. As expected, the Golgi apparatus redistributed to scattered structures of either circular shape or as short ribbons. In Fig. 7, A and B, GFP–COL is distributed through-

appear negative for the trans-Golgi (B; circles). Similar smaller structures are positive for GFP and the Golgi marker (asterisks) and follow the previously described phenotype of concentration of GFP–COL at the edge of the Golgi (t = 14–18 min), followed by filling of the Golgi (t = 23 min). **(C)** Image stills of a whole cell taken at one frame every 30 s (derived from Video 7). Accumulation and filling of the Golgi with GFP–COL occurs within t = 10.5 min. **(D)** Corresponding enlargements of the Golgi area in C. Channels are displayed separately in gray scale followed by a merge image. A total of n = 4 sets was acquired. For each set of live imaging experiments, three cells from the same dish were imaged simultaneously. Scale bars, 10 µm; in enlargements, 1 µm.
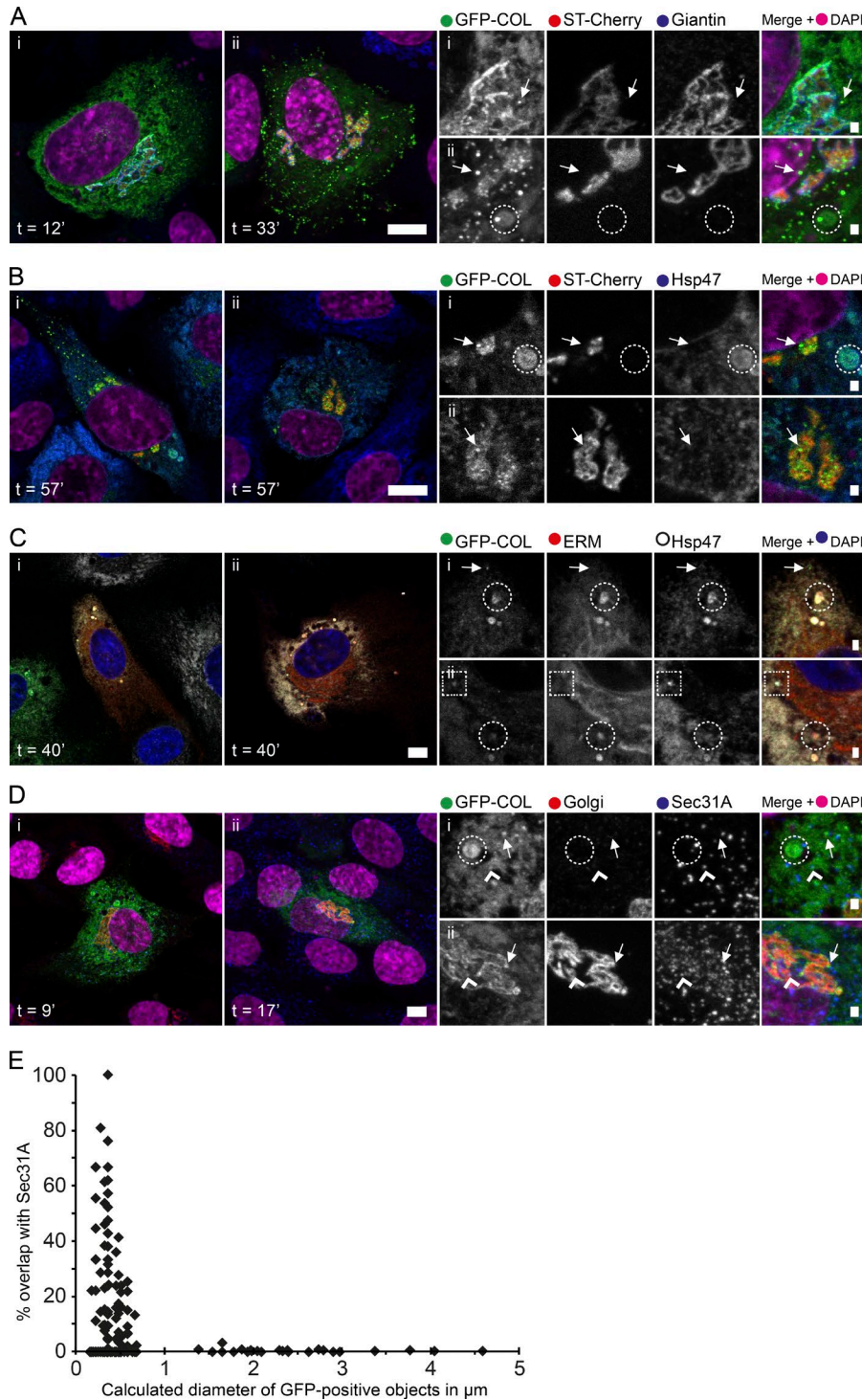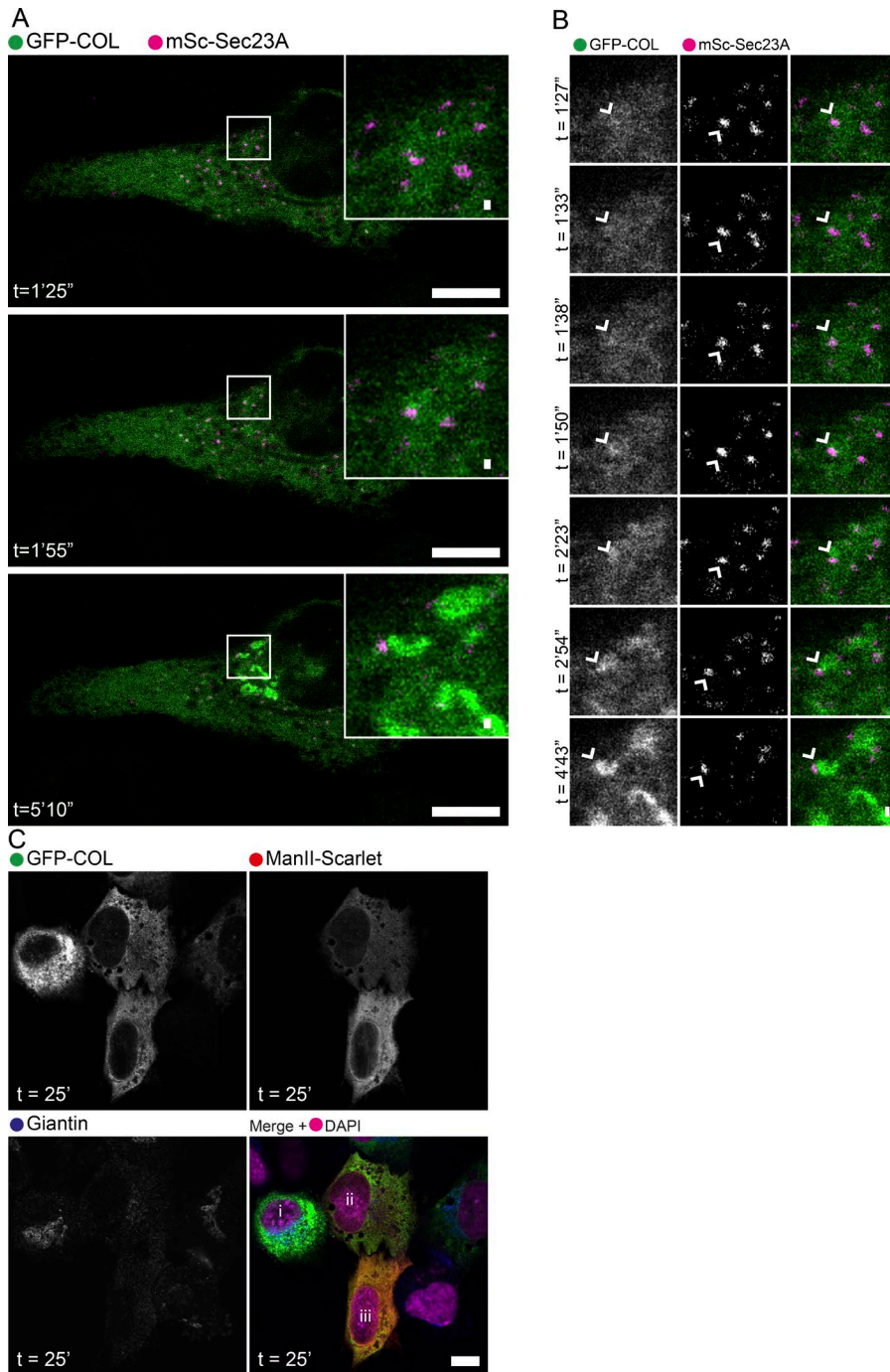
Figure 3. Large GFP–COL structures are positive for ER markers and Hsp47 but not COPII. Confocal imaging of RPE-1 cells stably expressing GFP–COL (green; GFP–COL–RPE) cotransfected with either ST-Cherry (red; A, B, D; 16–20 h after transfection) or the ER membrane marker ERM-mScarlet-i (red; C; 6–8 h after transfection). Cells were fixed after the given time points (minutes after addition of asc/biotin [500 µg·ml^{-1} and 400 µM, respectively]) and labeled after fixation with antibodies against further proteins of interest. Large panels show whole cells, while smaller panels show corresponding enlargements of areas of interest with the separate channels in gray scale, followed by the merge image including DAPI (acquired as separate channel and displayed in magenta in A, B, and D or blue in C). Scale bars, 10 µm; in enlargements, 1 µm. $n \geq$ 10. **(A)** Maximum projection images of z stacks containing the Golgi apparatus. Duration of asc/biotin corresponds to duration of prior live imaging at approximately one image every 30 s until trafficking of GFP–COL to the Golgi was detectable by eye. Cells were labeled with the cis/medial Golgi marker Giantin (blue). Image i (after corresponding Video 8, i) shows an accumulation of GFP–COL at the edge of the Golgi, without visible large GFP-positive structures. Small puncta can be observed in the cell periphery and close to the Golgi (images i and ii, arrows). Large GFP–COL-positive structures are negative for both the trans- and cis/medial-Golgi markers (image ii, circles). The corresponding video of live imaging before fixation of image ii is shown in Video 6 with image stills shown in Fig. 2, A and B. **(B)** Duration of asc/biotin corresponds to duration of prior live imaging at approximately one image every 30 s until trafficking of GFP–COL to the Golgi was detectable by eye (Video 8, ii). The GFP–COL within the ER at 57 min asc/biotin colocalizes with Hsp47 (blue) in the ER (images i and ii). The GFP–COL puncta in the cell periphery and close to the Golgi are negative for Hsp47 and the trans-Golgi marker ST-Cherry (arrows). Cells that show large (>1-µm diameter) GFP–COL-positive structures appear negative for the trans-Golgi but positive for Hsp47 (image i, circles). **(C)** Time point indicates incubation with 400 µg·ml^{-1} ascorbate before fixation. The GFP–COL colocalizes with the transiently expressed ERM-mScarlet-i (ERM; red) and Hsp47 (gray scale) in the ER, including large structures (images i and ii, circles). Small GFP-positive puncta, likely post-Golgi carriers, show no colocalization with ERM or Hsp47 (image i, arrows), while some small punctate GFP–COL structures are positive for Hsp47 but not ERM (image ii, square). **(D)** Maximum intensity projection images of z stacks of whole cells. Duration of asc/biotin corresponds to duration of prior live imaging at approximately one image every 30 s until trafficking of GFP–COL to the Golgi was detectable by eye (Video 8, iii and iv, respectively). The red channel marked as "Golgi" shows the combined signal from ST-Cherry and antibody-labeling for giantin in the same channel to enable complete visualization of the Golgi apparatus. Observed large GFP-positive structures do not colocalize with the COPII marker Sec31A (blue; image i, circles). Small GFP–COL puncta (<0.5 µm in diameter) close to the Golgi and in the cell periphery label for Sec31A (images i and ii, arrowheads). Most small punctate GFP-positive structures do not colocalize with Sec31A (images i and ii, arrows). **(E)** Size distribution of GFP-positive objects relative to colocalization with the COPII marker Sec31A from confocal z stacks with Δz = 0.29 µm and a sufficient number of slices to represent whole cells (as shown in D). The x axis shows the calculated object diameter of GFP-positive objects in micrometer, while the y axis shows the calculated percentage overlap of GFP-positive objects with Sec31A. Images for analysis were obtained after live-cell microscopy, as described in Figs. 1 and 2, and samples were fixed at the time when an accumulation of GFP–COL at the Golgi was visible by eye. In 11 of the 55 analyzed cells, no punctate or large GFP–COL objects were detected. These cells only show a GFP–COL accumulation around or in the Golgi. The remaining 44 cells show a total number of 1,149 detected objects in the GFP channel.

McCaughey et al.
ER-to-Golgi traffic of procollagen

Journal of Cell Biology
https://doi.org/10.1083/jcb.201806035

935

A
GFP-COL ● mSc-Sec23A ●

t=1'25"
t=1'55"
t=5'10"

B
GFP-COL ● mSc-Sec23A ●

t=1'27"
t=1'33"
t=1'38"
t=1'50"
t=2'23"
t=2'54"
t=4'43"

C
GFP-COL ● ManII-Scarlet ●

Giantin ● Merge + ● DAPI

t = 25'
t = 25'
t = 25'
t = 25'

Figure 4. **The GFP–COL transport is COPII dependent. (A and B)** Still images from confocal live-cell imaging of RPE-1 stably expressing GFP–COL (green; GFP–COL–RPE) cotransfected with the inner-layer COPII marker mSc-Sec23A (magenta) derived from Video 9. Acquisition at one frame every 2.79 s. Time points indicate time in presence of asc/biotin (500 µg·ml⁻¹ and 400 µM, respectively) and 20 h after transfection. Scale bars, 10 µm; in enlargements, 0.25; *n* = 9. **(A)** Large panels show the entire cell with enlargements displayed in the top right corner. **(B)** The zoomed in area of interest from A (also indicated by the square) with the separate channels in gray scale, followed by the overlay image. Arrowheads indicate a GFP–COL structure that colocalizes with an mSc-Sec23A structure and at ~1 min 38 s before the GFP–COL structure becomes part of the Golgi network. Scale bar, 0.25 µm. **(C)** Example image of GFP–COL–RPE cells cotransfected with ManII-mSc and the GTP-locked form of Sar1 (Sar1-H79G), which results in a COPII block. Panels show the separate channels GFP–COL (green) and MannII-mSc (red), as well as antibody labeling with a cis-Golgi marker giantin, in gray scale followed by the overlay image including nuclear labeling for DAPI (imaged as a separate channel in pseudocolor magenta). The time point indicates the incubation in presence of asc/biotin before fixation with PFA and 7.5 h after transfection. Scale bar, 10 µm. Cells expressing Sar1H79G show a scattered a disrupted Golgi apparatus, marked by ER labeling, compared with visible Golgi stacks in cells not affected by the COPII block (indicated by i). No transport of GFP–COL can be observed in COPII blocked cells (indicated by ii and iii).

out the ER, while two larger GFP–COL structures (diameter of ~1.5–2 µm) could be seen close to the nucleus with a signal intensity higher than that of GFP–COL in the ER background. In this example, GFP–COL structures are first visible, distributed throughout the cell, 19 min after addition of asc/biotin/NZ (Video 10). Nearly all structures appeared at the edge of the scattered trans-Golgi elements. Gradual accumulation of GFP–COL at the edge of the trans-Golgi further increased for ~4 min. No vesicular–tubular or circular transport carriers could be identified. An even distribution throughout the trans-Golgi could be observed between 26 and 35 min after addition of asc/biotin/NZ (depending on the individual Golgi element; Fig. 7, A and B; and

Video 10). The overall signal intensity for GFP–COL subsequently decreased over time. Once the trans-Golgi had filled, small GFP–COL puncta were seen emerging from Golgi elements and moving toward the cell perimeter. Subsequent emptying of the Golgi, consistent with onward trafficking of GFP–COL, was indistinguishable from traffic in the absence of NZ (Fig. 7 C, t = 44'14'').

Discussion

The currently accepted model for ER export of fibrillar procollagens, such as COL1A1, requires transport in large vesicles ranging in size from ~400 to 1,200 nm (Stephens, 2012; Miller and
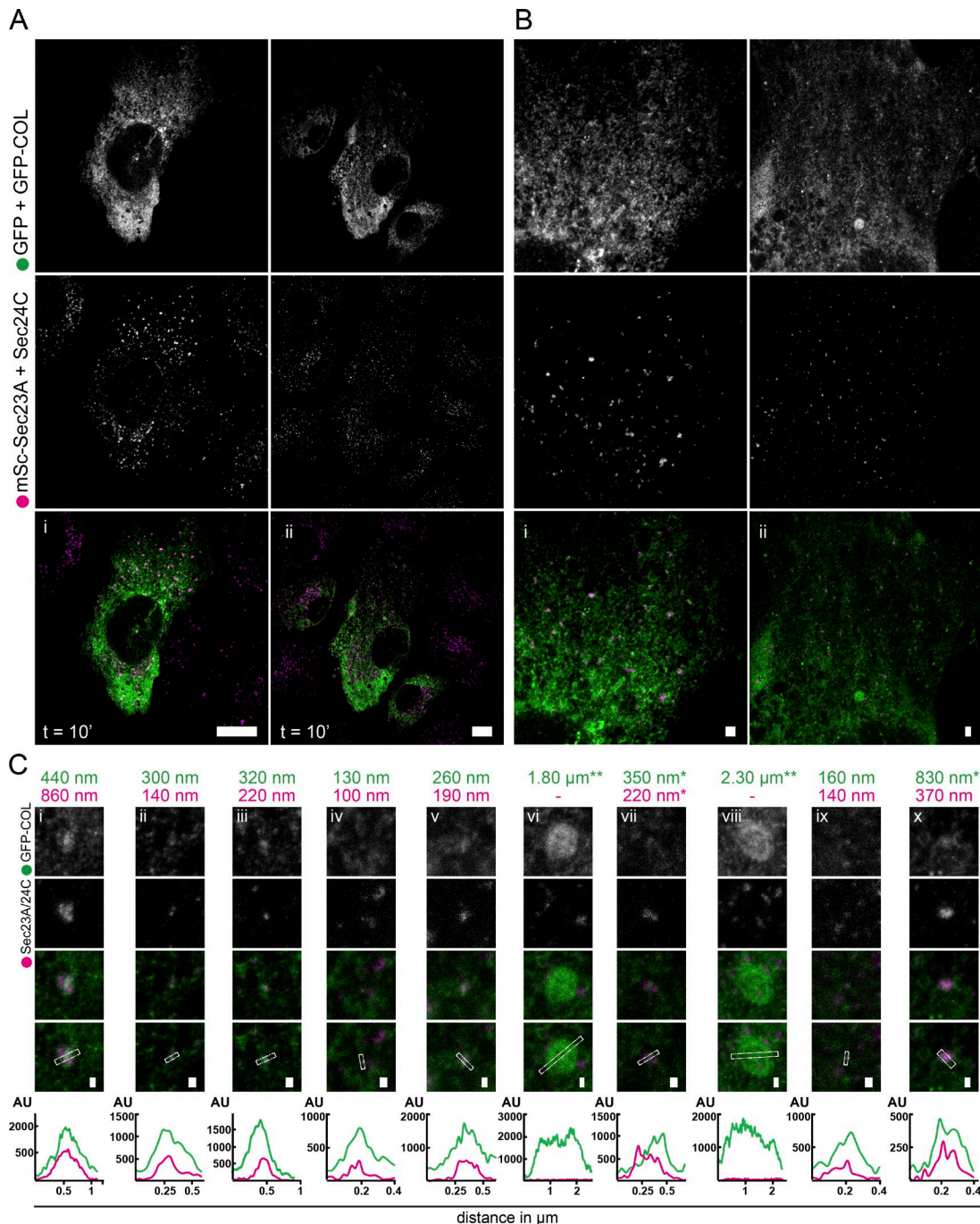
Figure 5.   **The GFP–COL puncta colabeling for the inner COPII layer do not exceed 450 nm in diameter. (A)** Confocal images obtained using STED micros-copy of whole RPE-1 cells stably expressing GFP–COL (GFP–COL–RPE; colabeled with an antibody against GFP in the same channel; green) cotransfected with the inner layer COPII-marker mSc-Sec23A and additionally colabeled with an antibody against Sec24C in the same channel (magenta). Time points indicate incubation in presence of asc/biotin (500 µg·ml^{-1} and 400 µM, respectively) before fixation with PFA. Scale bar, 10 µm; *n* = 14. **(B)** Corresponding zoomed in areas of the cells in A, obtained using superresolution microscopy (gSTED). Scale bar, 1 µm. **(C)** Enlargements of small GFP-positive puncta colocalizing with the COPII marker and large GFP-positive structures extracted from images as displayed in B. Panels show the different channels in gray scale, followed by the overlay image and the overlay image containing the line with a width of 5 (images ii–v, vii, and ix) or 10 pixels (images i, vi, viii, and x) drawn through the object of interest to generate the corresponding line graphs, as shown below. Line graphs display the distance in micrometers on the x axis and the signal intensity as an au on the y axis. The FWHM values corresponding to the estimated maximum object diameters in nanometers or micrometers are displayed above the images for the corresponding line graphs fitted with a Gaussian curve (in green for GFP + GFP–COL and in magenta for mSc-Sec23A + Sec24C). When two curves were used to fit the graphs, the sum of the FWHM was used as an estimate (indicated by asterisk). When Gaussian fitting was not possible, the displayed estimated diameter value was measured via ImageJ (two asterisks). If no peak in the red channel could be identified, values were left blank (indicated by dash).
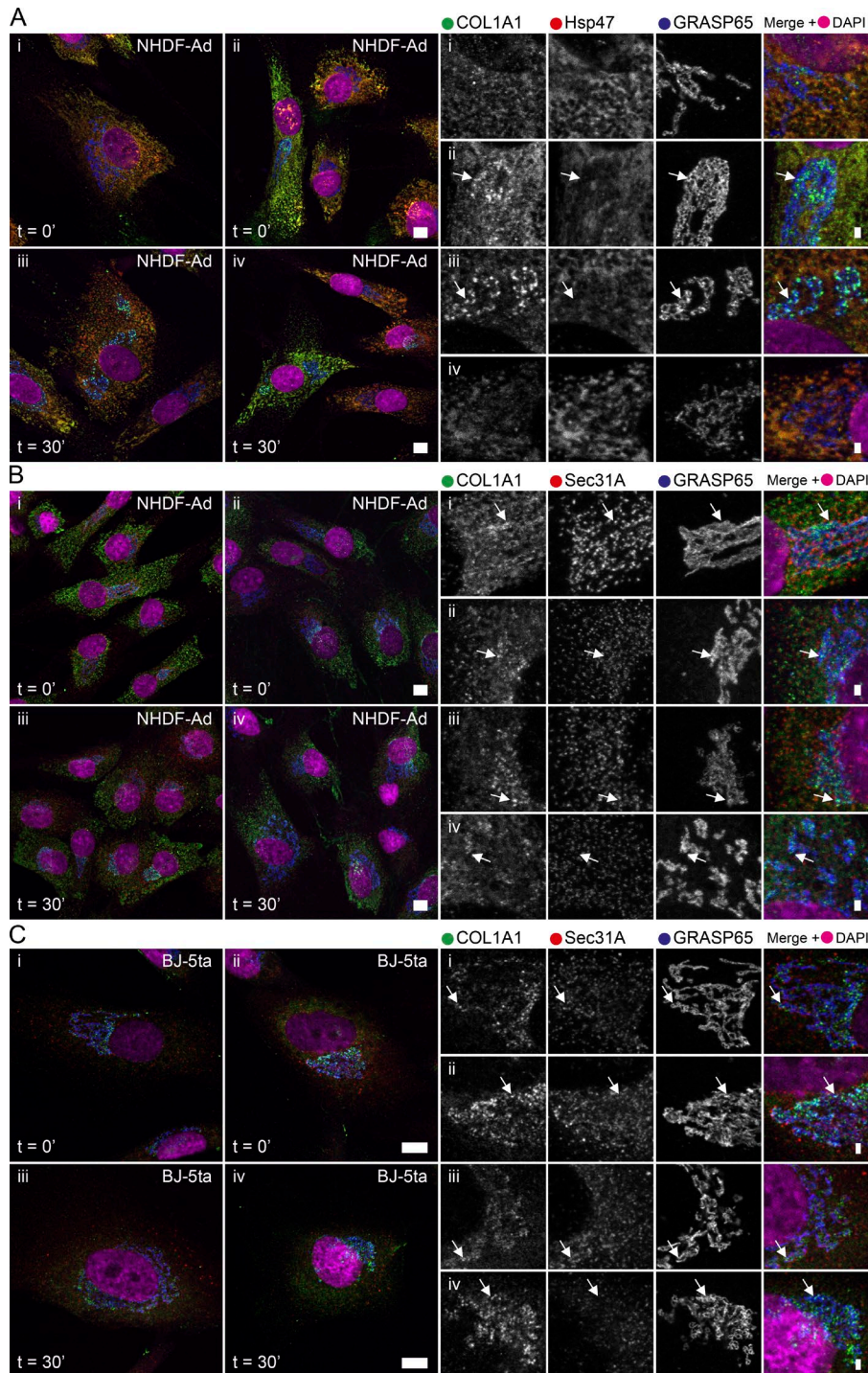
Figure 6. In primary fibroblasts, endogenous procollagen colocalizes with Hsp47 in the ER. Confocal images of cells after incubation in the presence of 500 μg·ml⁻¹ ascorbate (A and B) or 50 μg·ml⁻¹ ascorbate (C) for 0 (images i and ii) and 30 min (images iii and iv), respectively. **(A and B)** Maximum intensity projection images of z stacks through primary adult skin fibroblasts NHDF-Ad. **(C)** Shows single z slice images of nontransformed foreskin fibroblasts (BJ-5ta). Cells were labeled using antibodies against COL1A1 (green) and either Hsp47 (A) or the COPII marker Sec31A (B and C) in red, as well as a cis-Golgi marker GRASP65 (blue). Panels show whole cells, as well as corresponding enlargements of the Golgi area on the right. Enlargements show the separate channels in gray scale as well as the overlay image including nuclear staining in magenta (DAPI, imaged as separate channel). Arrows highlight punctate COL1A1 structures with high signal intensity localizing in close proximity to the Golgi. Scale bars, 10 μm; in enlargements, 1 μm. The NHDF-Ad show varying expression levels of Hsp47 and COL1A1 (A, images i–iv). Localization of COL1A1 to punctate structures in the Golgi area occurs at both 0 and 30 min in the presence of ascorbate (A, images ii and iv, and B, images i–iv, arrows). The BJ-5ta show lower levels of COL1A1 expression compared with NHDF-Ad, but accumulation of COL1A1 in the Golgi area can also be observed at both time points (C, images i–iv, arrows). $n \geq 10$ in each case.

Schekman, 2013; Venditti et al., 2014; Malhotra and Erlmann, 2015; Saito and Katada, 2015). There are several reports of these structures in the literature from both cell-based and in vitro experiments (Jin et al., 2012; McGourty et al., 2016; Gorur et al., 2017; Yuan et al., 2017). Our data, using both stable expression of a newly engineered fluorescent procollagen reporter and endogenous labeling, do not support that model, at least for the long-range translocation of carriers from the peripheral ER to the Golgi. Analysis of fixed cells shows that, where detected, most carriers are <350 nm in size. We also do not detect large structures that are COPII coated. However, live-cell imaging does not

support a model where these are a major component of ER-to-Golgi trafficking. In contrast, our work shows that GFP–COL accumulates at sites juxtaposed to the Golgi without the formation of large carriers. Analysis of endogenous procollagen trafficking in fibroblasts confirmed this observation.

The construct we describe here is tagged at the N terminus before the protease cleavage site. Very recently, similar constructs where the α2 chain of type I procollagen (COL1A2) was tagged at the N terminus were described (Lu et al., 2018). In that work, the N-terminal propeptide was replaced with a fluorescent protein, and the cleavage site was removed intentionally, to enable
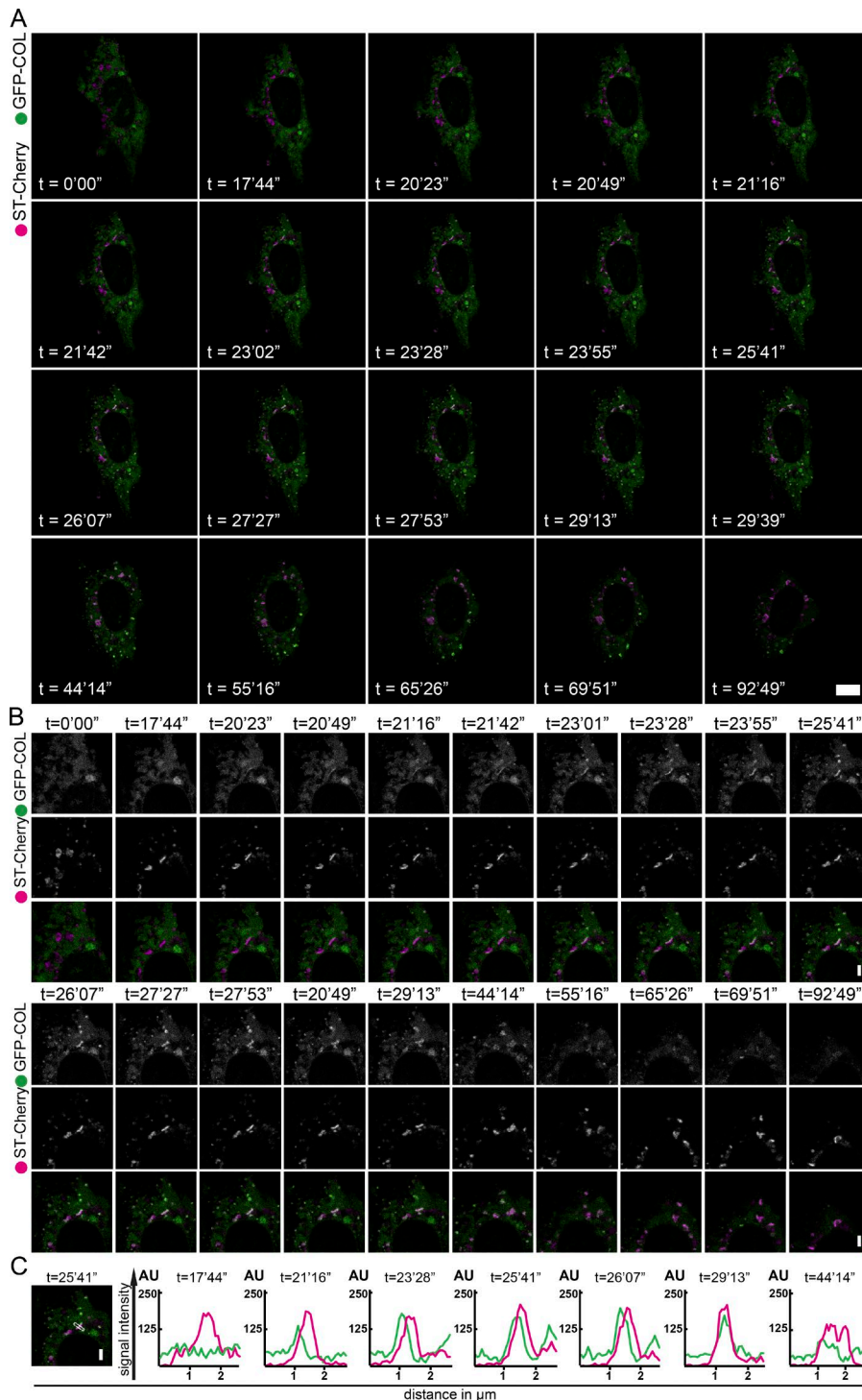
Figure 7. **GFP–COL trafficking does not rely on an intact microtubule network.** Still images from confocal live-cell imaging of RPE-1 stably expressing GFP–COL (green; GFP–COL–RPE) cotransfected with the trans-Golgi marker ST-Cherry (magenta) derived from Video 6. Acquisition at one frame every 26 s. Cells were incubated in presence of NZ for 60 min before imaging. Time points indicate time in presence of asc/biotin (500 µg·ml^{-1} and 400 µM, respectively). **(A)** Large panels show the entire cell. Scale bar, 10 µm. **(B)** Enlargements highlight a zoomed in area of interest. Small panels show the green channel and magenta channel in gray scale followed by the overlay. Scale bar, 1 µm. **(C)** Example image of an enlarged overlay with a 5-pixel-wide line drawn through the Golgi followed by corresponding line graphs of selected time points showing the signal intensity (y axis) in arbitrary units for GFP–COL (green) and ST-Cherry (magenta) for the corresponding line. The x axis shows the distance in micrometers. $n = 4$.

the visualization of procollagen in the ECM. In our construct, we chose to retain the cleavage site such that the extracellular procollagen itself did not become fluorescent, thus enabling us to image intracellular trafficking more effectively. Furthermore, atypical retention of the N-propeptide due to impaired cleavage can lead to pathologies that overlap with those of osteogenesis imperfecta and Ehlers–Danlos syndrome (Cabral et al., 2005; Malfait et al., 2013). Another recent development has been the engineering of a photoactivatable Dendra2 fluorescent protein into the endogenous locus of COL1A2 (Pickard et al., 2018 *Pre-print*). Here, Dendra2 was placed after the N-terminal cleavage site such that it is also retained in extracellular collagen fibrils. While this has advantages in terms of endogenous tagging and in analysis of fibril turnover, it does not enhance the ability to control ER export or to selectively analyze intracellular precursors versus extracellular pools.

A major caveat to the use of fluorescent protein–tagged reporters of procollagen is the question of how much of the visualized reporter is indeed trimeric, assembled procollagen. We chose to tag COL1A1 rather than COL1A2 because of its capacity to

homotrimerize (Jimenez et al., 1977; Uitto, 1979), potentially lessening the effect of overexpression. We have validated that GFP–COL can and indeed does heterotrimerize with COL1A2 in RPE-1 cells using proteomics (Fig. S5 B). However, it should be noted that our own RNaseq data (Stevenson et al., 2017) has shown that COL1A2 is only expressed at very low levels in these cells (shown in table form in Fig. S5 C). The simplest interpretation is that the COL1A1 homotrimer is therefore the relevant trimer in these cells. We also showed that our stable expression of GFP–COL does not significantly affect expression of COPII proteins including Sec31A, Sec12, TFG, Sec24A, or Sec24C (Fig. S5 D). In addition, we did not detect major differences in the total amount of COL1A1 expressed by these cells (Fig. S5 E). We consider it important to note that we, and others, using reporters of this type, likely visualize a combination of monomeric and trimeric procollagen exiting the ER. The ascorbate dependence of ER exit supports the idea that a major pool is indeed trimeric. Regardless, we have not observed large procollagen-containing structures, COPII-coated or otherwise, in any significant number that could mediate the transport of procollagen from the ER to Golgi.

Our work supports the possibility of direct connections between the ER and Golgi to facilitate transfer of folded procollagen (Kurokawa et al., 2014; Malhotra and Erlmann, 2015). This idea has parallels with the cisternal maturation model of procollagen Golgi transit, where procollagen does not make use of vesicles while trafficking between Golgi stacks but rather stays within the cisternae (Bonfanti et al., 1998). Direct connections are difficult to envisage given the well-characterized differences in composition between these organelles. A model that could reconcile this is the local formation of budding structures at ERES in close proximity to Golgi membranes (Fig. 8), as have been generated in in vitro budding assays (Gorur et al., 2017; Yuan et al., 2017). Direct connection of the ER to the ERGIC would both prevent compartment mixing of the ER and Golgi and be consistent with data on the role of TANGO1 (Nogueira et al., 2014; Ma and Goldberg, 2016; Raote et al., 2018). One could view such a model as a maturation process where these nascent COPII-coated carriers from the ERGIC itself acquire compartment-specific markers and identity by direct fusion (Fig. 8 B). This is also consistent with the NZ experiments in which the Golgi is distributed adjacent to peripheral ERES. However, there is no direct evidence of such direct connections or for an equivalent of cisternal maturation from the ERGIC to early Golgi.

This model raises questions about how large procollagen molecules could be encapsulated in COPII vesicles. Recent new data have challenged previous assumptions concerning the rigidity of triple helical collagen (Rezaei et al., 2018), showing instead that it can best be described as a semiflexible polymer. Atomic force microscopy showed that the global curvature of collagen varies greatly with the salt concentration and pH. This was seen with many collagen isotypes. It is therefore not inconceivable that the conditions at the point of ER exit are consistent with flexible procollagen that could be packaged into vesicular carriers closer in size to those classically described for COPII.

In many cases, small GFP–COL puncta were seen in our experiments that colocalize with Sec31A. These show a distinct size distribution from large, static, circular structures negative

for the COPII marker. Therefore, our data are entirely consistent with COPII-dependent trafficking of procollagen from the ER via conventionally described ERES, and we do not dispute an absolute requirement for COPII in this process. Indeed, there is overwhelming support for this from in vitro (Gorur et al., 2017; Yuan et al., 2017), cell-based (Stephens and Pepperkok, 2002; Townley et al., 2008), and whole-animal experiments (Lang et al., 2006; Townley et al., 2008; Garbes et al., 2015).

Our work also shows that trafficking and secretion of GFP–COL does not require an intact microtubule network. Transport of GFP–COL to Golgi stacks in our experiments appeared very similar to that of GFP-tagged tumor necrosis factor (TNF-SBP-EGFP; Fourriere et al., 2016), supporting the idea that this pathway might not be restricted to procollagen or other large cargo. We also think it unlikely that this short-loop pathway is itself mediated by the formation of large carriers, because large structures of the type described by others (Jin et al., 2012; McGourty et al., 2016; Gorur et al., 2017; Raote et al., 2017) are not evident in our experiments analyzing either fixed or live cells. Notably, in those previously published experiments, COPII labeling appears very different from what one might expect from many other studies with few structures evident (Jin et al., 2012). Live imaging of both Sec31A-YFP and procollagen-CFP in KI6 cells that overexpress both procollagen and KLHL12 shows limited movement of an apparent Sec31A-positive and procollagen-positive structure over ∼3 min (Gorur et al., 2017). This finding is not entirely consistent with long-range, vectorial ER-to-Golgi transport described previously (Stephens and Pepperkok, 2002), and the highly dynamic nature of the ER itself must be considered. Some large FLAG-KLHL12- and Sec31A-positive structures in KI6 cells colocalize with Hsp47 (Gorur et al., 2017). These structures would be consistent with our larger GFP–COL structures that are also positive for the collagen chaperone Hsp47.

In our experiments, some larger procollagen-containing structures are visible, but our data show that these are most likely domains within the ER as they colabel for an ER membrane marker and Hsp47. Being contiguous with the ER, one might expect that these would label with markers of ERES, which are normally highly abundant in cells. Notably, we do not observe substantial labeling of these structures with Sec31A. The trafficking of Hsp47 itself is somewhat unclear. While it can bind to both monomeric and trimeric procollagen (Satoh et al., 1996) and has a KDEL retrieval sequence, both consistent with export from the ER, its localization at steady state is almost entirely restricted to the ER (Kano et al., 2005; Duran et al., 2015; Salo et al., 2016). Current models favor a role for Hsp47 in maintaining the procollagen trimers in a nonaggregated state within the ER (Tasab et al., 2000) and possibly during further transit through the secretory pathway. In vitro data show that Hsp47 preferentially binds to the trimeric form of procollagen (Tasab et al., 2002; Koide et al., 2006; Ono et al., 2012; Ishikawa et al., 2016; Ito and Nagata, 2017) and accompanying procollagen after release from the ER (Satoh et al., 1996; Oecal et al., 2016). Interestingly, while most GFP–COL puncta in the cell periphery, as well as those close to the Golgi, were negative for Hsp47, some of these small punctate structures were positive for Hsp47 while also being negative for ER membrane. Therefore, these structures could be bona fide ER-to-Golgi transport carriers.
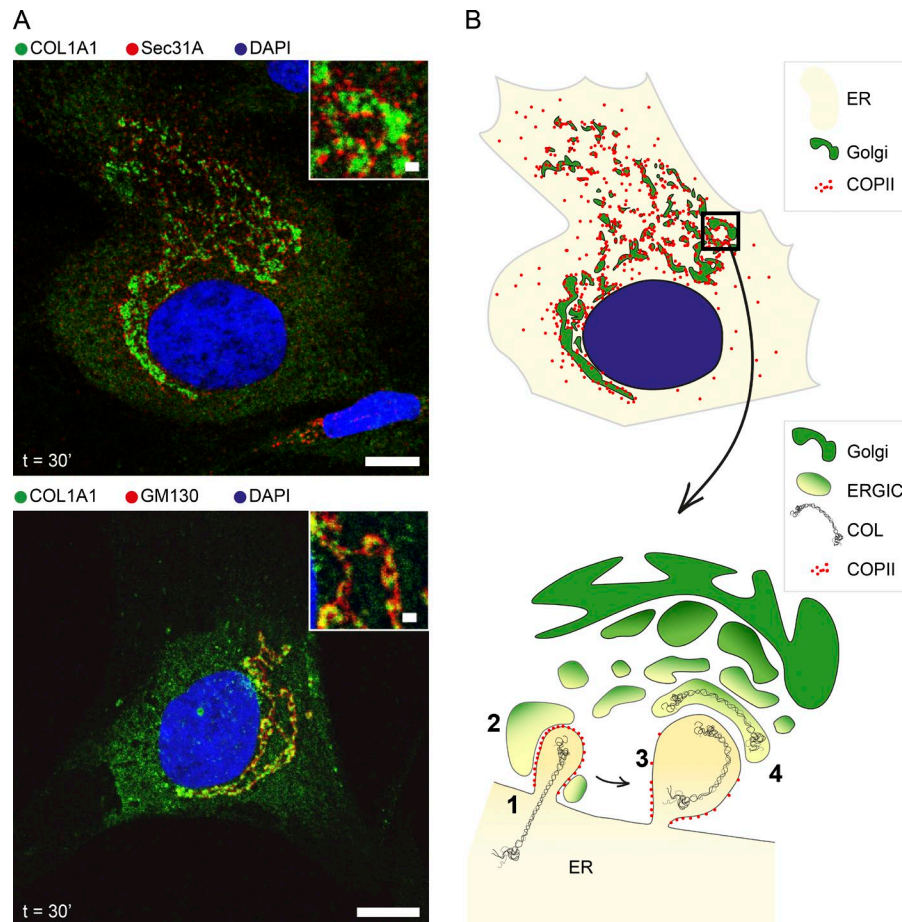
Figure 8. **The GFP–COL transport to the Golgi via a "short-loop" pathway. (A)** Immunofluorescence image of a primary skin fibroblast labeled for (1) endogenous COL1A1 (green) and Sec31A (red) and (2) endogenous COL1A1 (green) and GM130 (red), both after 30-min incubation in presence with 50 µg·ml⁻¹ ascorbate. Scale bars, 10 µm; in enlargements, 1 µm. **(B)** Schematic of a cell with zoomed in region showing COL1A1 transport from ERERS in close proximity to the Golgi. (1) COPII-dependent packaging of procollagen into nascent buds. (2) These buds are expanded by TANGO1-dependent fusion with the ERGIC. (3) Carrier expansion encapsulates procollagen. Questions remain as to the extent of expansion required and the flexibility of the trimer at this stage. (4) Scission of the carrier generates a compartment that almost immediately adopts the identity of the ERGIC and progresses to become the first cisterna of the Golgi. In this model, the ERGIC acts as an intermediate to both expand the nascent ER-derived carrier and to ensure compartmentalization of ER and Golgi.

Mechanistically, a complex machinery, including KLHL12, is clearly involved in COPII-dependent trafficking from the ER. Our data, however, suggest that its role is not to generate large carriers in the cell periphery to direct this traffic. Rather, our findings indicate that procollagen trafficking utilizes what we term a short-loop pathway from the ER to the Golgi. This pathway could of course be used by other cargo. Advances in both light and EM provide opportunities to address this further. However, we conclude from our work that large carriers do not mediate long-range transport of procollagen from the peripheral ER to the Golgi.

Materials and methods

Unless stated otherwise, all reagents were purchased from Sigma-Aldrich.

DNA constructs

All restriction and modifying enzymes were purchased from New England Biolabs. The ER-membrane marker pCytERM_mS-

carlet-i_N1 was a gift from Dorus Gadella (University of Amsterdam, Amsterdam, Netherlands; Addgene; plasmid no. 85068; Bindels et al., 2017). mCherry-LC3B was a gift from Jon Lane (University of Bristol, Bristol, UK; the GFP tag from GFP-LC3B [Betin et al., 2013], pLXG-3 SSFFV GFP-LC3B, was replaced by the Lane laboratory for an mCherry tag). To generate the Str-KDEL-IRES-ST-mCherry (Addgene; no. 110727) construct, Str-KDEL_ST-SBP-mCherry (Addgene; no. 65265), a gift from Franck Perez (Institut Curie, Paris, France; Boncompain et al., 2012), was used as a template; the ST-SBP was exchanged for an ST sequence without the SBP tag via restriction digest with AscI and SbfI. To generate Str-KDEL-IRES-mannosidaseII-mScarlet-i (MannII-mSc; Addgene; no. 117274) and Str-KDEL-IRES-mScarlet-i-Sec23A (Addgene; mSc-Sec23A; no. 117273), Str-KDEL-IRES-mannosidase II-SBP-mCherry (Addgene; no. 65253), a gift from Franck Perez (Boncompain et al., 2012), and mScarlet-i (Addgene; no. 85044), a gift from Dorus Gadella (Bindels et al., 2017), were used as a template. For MannII-mSc, the SBP-mCherry tag was replaced with mScarlet-i. For mSc-Sec23A, mannosidaseII-SBP-mCherry were first replaced with mScarlet-i and in a second step Sec23A

from pLVX-Puro-mRuby-Sec23A (Addgene; no. 36158; Hughes and Stephens, 2010) was amplified using PCR and inserted after Str-KDEL-IRES-mScarlet-i. Sar1-H79G was described previously (Aridor et al., 1995).

The GFP–COL construct was designed using the New England Biolabs assembly tool to introduce a SBP-mGFP tag between the N-propeptide and the corresponding cleavage site upstream of the triple helical domain of human procollagen 1α1. This tagging was realized by using a two-step NEB HiFi Assembly reaction. First, the inserts procollagen-SBP, a synthetic construct composed of the sequence encoding the signal peptide and N-propeptide of human procollagen 1α1 (synthesized by MWG in pEX-A2), humanized mGFP (equivalent to NCBI accession no. KP202880.1), and the genetic sequence encoding the triple helical domain and the C terminus of human COL1A1 (NCBI accession no. NM_000088.3) were amplified via PCR (primers listed below). mGFP and COL1A1 were subsequently purified via gel extraction. Prior to assembly, the remaining template vector procollagen-SBP-pEX-A2 was digested using DpnI. The lentiviral vector backbone pLVXPuro (Takara Bio Europe) was linearized via overnight digest with EcoRI and subsequent heat inactivation. For the reaction the compounds to be combined were added in equimolar proportions of 0.05 pmol, except for procollagen-SBP with 0.18 pmol, and incubated with the assembly master mix for 3 h at 50°C, according to the NEB HiFi Assembly protocol. The transformation of NEB 5α competent *Escherichia coli* was performed as described in the protocol. Sequencing of clones after the first assembly reaction showed successful insertion of mGFP and COL1A1 into pLVXPuro and an introduction of a unique *Psh*AI restriction site between pLVXPuro and mGFP, which was used for a second assembly reaction. For this, 0.04-pmol procollagen-SBP, amplified using the primers listed below, and 0.02 pmol of the first assembly product (linearized using PshAI) were used for the assembly reaction. Resulting colonies yielded the desired construct procollagen-SBP-mGFP-COL in pLVXPuro (GFP–COL; Addgene; no. 110726).

Primers (synthesized by Sigma-Aldrich) used for amplification of the inserts are as follows: forward primer for mGFP, 5′-AGAGCCCATGTGCTGCTGCTGCATGGTGAGCAAGGGCGAG-3′; reverse primer for mGFP, 5′-GGGGCAGCAGCAGCACTTGTACAGCTCGTCCATGC-3′; forward primer for COL1A1, 5′-GCTGTACAAGTGCTGCTGCTGCCCCCAGCTGTCTTATGGC-3′; reverse primer for COL1A1, 5′-CGCGGTACCGTCGACTGCAGTTACAGGAAGCAGACAGG-3′; and final primers for procollagen-SBP amplification, 5′-ACTCAGATCTCGACACCGGTCGCCACCATGTTCAGCTTTG-3′ (forward) and 5′-CCATGGTGGCGACCGGTGTCTTCATGGGCTCTCTCTGG-3′ (reverse).

Cell culture, cell lines, and transfection

All cells were cultured at 37°C and 5% CO_2 in a humid environment. The IMR-90 (ATCC; CCL-186) were grown in MEM (Sigma-Aldrich) supplemented with L-glutamine and 10% decomplemented FBS (Gibco). The DMEM (Gibco) containing 2% M199 (Gibco) and 10% decomplemented FBS was used for cell culture of BJ-5ta hTERT-immortalized fibroblasts (ATCC; CRL-4001). The NHDF-Ad-Der (NHDF-Ad) primary fibroblasts (Lonza cat. no. CC-2511) were grown in fibroblast basal medium supplemented with fibroblast growth medium-2 (Lonza). For generating the cell line stably expressing the GFP–COL construct, as well as a cell line expressing just GFP as a control, hTERT RPE-1 cell line (ATCC; CRL-4000) were used. These cells were grown in DMEM-F12 Ham (Sigma-Aldrich) supplemented with 10% decomplemented FBS. Cells were not validated after purchase but were routinely screened annually (and confirmed negative) for mycoplasma contamination.

To make the stable GFP–COL cell line, virus containing the GFP–COL construct was generated using the Lenti-XTM Packaging Single Shots (vesicular stomatitis glycoprotein pseudotyped version) system from Takara Bio Europe according to the manufacturer's instructions (631275). Growth medium was removed from an 80% confluent 6-cm dish of hTERT-RPE-1, and 1 ml harvested virus supernatant supplemented with 8 µg·ml⁻¹ polybrene was added to cells. After 1 h of incubation at 37°C and 5% CO_2, 5 ml growth medium was added. Transfection medium was then replaced with fresh growth medium after 24 h. To select for transfected cells, cells were passaged in growth medium supplemented with 5 µg·ml⁻¹ puromycin dihydrochloride (Santa Cruz Biotechnology) 72 h after transfection. The hTERT-RPE-1 cells stably expressing GFP (GFP–RPE) were generated previously (Asante et al., 2014). Stable cell lines were maintained in growth medium containing 3 µg·ml⁻¹ puromycin.

Cells were transfected at 80% confluence according to the manufacturer's protocol (Thermo Fisher Scientific) but using 2.5 µl Lipofectamine 2000 transfection solution (Invitrogen), 1 µg plasmid DNA, and 250 µl OPTIMEM per 35-mm well, added dropwise onto the cells with 1 ml of fresh medium. Transfection with ST-Cherry, GFP–COL, ManII-mSc, or mSc-Sec23A was performed ∼16–20 h before fixation or live imaging, while transfection with ERM or Sar1-H79G was performed 6–8 h before the procollagen-trafficking experiments.

Immunofluorescence

For immunofluorescence, cells were grown on 13-mm coverslips (0.17-mm thickness 1.5; Thermo Fisher Scientific) and fixed for 15 min at RT with 4% PFA (Thermo Fisher Scientific) at RT. For fixation after live imaging, cells were grown in live-cell dishes (MatTek Corp.) and fixed by adding 8% PFA to an equal amount of FluoroBrite DMEM imaging medium (Life Technologies; A18967-01). Cells were permeabilized with 0.1% (vol/vol) Triton X-100 (Sigma-Aldrich) for 10 min at RT and blocked with 3% BSA (Sigma-Aldrich) for 30 min. Immunolabeling with primary and secondary antibodies was performed at RT for 1 h in a humid environment and in the dark. Antibodies were diluted as follows in blocking solution to the final working concentrations or dilutions: 2.5 µg·ml⁻¹ for rabbit polyclonal anti-ATG16L (PM040; MBL), 0.5 µg·ml⁻¹ rabbit polyclonal anti-COL1A1 (NB600-408; Novus Biologicals), 1:250 for rabbit polyclonal anti-N- and C-propeptide of COL1A1 LF39 andLF41 (both gifts from Larry Fisher, National Institutes of Health, Bethesda, MD; Fisher et al., 1995), 5 µg·ml⁻¹ mouse monoclonal COL1A1–C-terminal antibody 3391 (clone 5D8-G9; Merck; MAB3391), 0.09 µg·ml⁻¹ mouse monoclonal anti–N-terminal collagen type I (Sp1.D8; DSHB), 10 µg·ml⁻¹ for anti–COL1A1-C-peptide (PIP) no. 42024 and no. 42043 (QED Biosciences), 1.25 µg·ml⁻¹ for mouse-monoclonal

McCaughey et al.
ER-to-Golgi traffic of procollagen

Journal of Cell Biology
https://doi.org/10.1083/jcb.201806035

942

anti-EEA1 (Clone 14/EEA1 [RUO]; BD Transduction Laboratories; 610456), 0.5 µg·ml^{-1} mouse monoclonal anti-GFP (MMS-118P; Covance), 1:2,000 for rabbit polyclonal anti-giantin (Poly19243; BioLegend), 0.25 µg·ml^{-1} mouse monoclonal anti-GM130 (BD Biosciences; 610823), 1:1,500 sheep polyclonal anti-GRASP65 (gift from Jon Lane), 0.75 µg·ml^{-1} mouse monoclonal anti-Hsp47 (M16.10A1; ENZO), 2 µg·ml^{-1} for rabbit polyclonal anti-Rab11 (Sigma-Aldrich; R5903), 1:250 for rabbit polyclonal anti-Sec24C ([Townley et al., 2008](#)) and 1:100 for Sec24D ([Palmer et al., 2005](#)), 0.25 µg·ml^{-1} mouse monoclonal anti-Sec31A (612350; BD Biosciences); 1:500 for mouse-monoclonal anti-transferrin receptor (TfR; clone H68.4; Thermo Fisher Scientific; 13-6800), and 2.5 µg·ml^{-1} for mouse-monoclonal anti-WIPI2 (clone 2A2; Bio-Rad; MCA5780GA).

Samples were rinsed three times with PBS for 5 min after incubation with primary and secondary antibodies. As secondary antibodies, 2.5 µg·ml^{-1} donkey anti-rabbit Alexa-Fluor-568–conjugated, donkey anti-mouse Alexa-Fluor-647–conjugated, or donkey anti-sheep Alexa-Fluor-488–conjugated antibodies were used. For labeling of endogenous procollagen donkey anti-rabbit Alexa-Fluor-488 conjugate was used.

Samples were washed with deionized water and mounted using ProLong Diamond Antifade with DAPI (Invitrogen) for confocal imaging or MOWIOL 4-88 (Merck-Millipore) mounting media for widefield imaging. Samples fixed after live imaging were incubated with DAPI (Invitrogen) for 3 min at RT before repeated washing and storage in PBS at 4°C in the dark until further imaging.

To show the effective disruption of microtubules after incubation with 5 µM NZ for 60 and 120 min, GFP–COL–RPE were fixed with –20°C methanol for 4 min, before blocking and immunofluorescent labeling with mouse monoclonal anti–α-tubulin antibody (1:1,000, clone B-5-1-2, T5168) and subsequent steps as described above.

Procollagen-trafficking experiments and image acquisition

The GFP–COL–RPE-1 were incubated in medium containing 50 µg·ml^{-1} L-ascorbic acid-2-phosphate (Sigma-Aldrich; termed ascorbate throughout) for 24–48 h before live image acquisition or fixation, to flush out overexpressed GFP–COL before a controlled accumulation in the ER for 24 h. Finally, to synchronize procollagen trafficking in GFP–COL–RPE, medium was supplemented to contain 500 µg·ml^{-1} ascorbate during live imaging or before fixation. This higher concentration was found to more effectively synchronize export. Experiments performed with cells cotransfected with an ER hook (ST-mCherry, MannII-mSc, or mSc-Sec23A, to use the RUSH system) were conducted 16–20 h after transfection, and the medium contained 500 µg·ml^{-1} ascorbate, as well as 400 µM biotin (Sigma-Aldrich), to enhance synchronization and trigger GFP–COL release in a time-dependent manner. For analysis of the dependence on the microtubule network, cells were treated as mentioned above but incubated in presence of 5 µM NZ for 60–120 min before the initiation of the trafficking experiment via addition of asc/biotin/NZ to the cells.

Images of cells transiently expressing GFP–COL were obtained through widefield microscopy using an Olympus IX-71 inverted microscope combined with Exfo Excite xenon lamp illumination, single-pass excitation and emission filters combined with a multipass dichroic (Semrock) and images captured on an Orca-ER CCD (Hamamatsu). The system was controlled using Volocity (v. 5.4.1; Perkin-Elmer). Chromatic shifts in images were registration corrected using TetraSpek fluorescent beads (Thermo Fisher Scientific).

All other images were obtained using confocal microscopy using Leica SP5II for fixed or Leica SP8 for live samples. The Z stacks of fixed samples labeled with Sec31A were acquired with Δz = 0.29 µm. For live-cell imaging, FluoroBrite DMEM (Thermo Fisher Scientific) was used as imaging medium. Live-cell imaging was performed using a Leica SP8 confocal laser scanning microscope with 63× HC OL APO CS2 1.42 numerical aperture glycerol lens and an environmental chamber at 37°C with CO$_2$ enrichment and Leica LAS X software. Fluorophores were excited using ≤2% energy of the 65-mW Argon laser at 488 nm for the green and a 20-mW solid state yellow laser at 561 nm for the red channel, respectively. Time courses were acquired using the sequential scanning mode between lines, imaging speed set to 700 Hz, 2× zoom, and detection of the green and the red channel using hybrid GaAsP detectors and corresponding notch filters. Each frame was acquired with a 3× line average. One to three cells per sample were chosen that showed low to moderate expression of both GFP–COL and ST-Cherry (estimated by eye) and imaged using multiposition acquisition with adaptive focus control active for each cycle and each position to correct axial drift between frames. Minimization of time between frames was undertaken to allow the highest temporal resolution possible with the given positions per sample resulting in intervals of 15–30 s between time points. Acquisition with a temporal resolution of one to three frames per second was accomplished by using a single position imaged at 2× line averaging, imaging speed set to 1,000 Hz and the highest zoom factor possible to capture a whole cell.

All images shown were not altered from the raw data, unless mentioned. Videos and video stills were enhanced in brightness and contrast for both channels, by using ImageJ autocorrection (except [Fig. 1 D](#)). All videos including imaging of ST-Cherry or MannII-mSc were registration corrected using ImageJ's built-in 3D correction for drifting, applied using the Golgi channel. All movies were smoothed using ImageJ's in-built smooth processing function.

Superresolution microscopy

The GFP–COL–RPE were cotransfected with mSc-Sec23A and after 24 h in presence of 50 µg·ml^{-1} ascorbate followed by 24-h ascorbate starvation and addition of 500 µg·ml^{-1} asc and 400 µM biotin 10 min before fixation with PFA as described previously. Samples were labeled with antibodies against GFP (mouse), as well as anti-Sec24C (rabbit). Donkey anti-rabbit Alexa-Fluor-568–conjugated antibody and donkey anti-mouse Alexa-Fluor-488–conjugated secondary antibodies were used, and samples were mounted with Prolong Diamond without DAPI (Thermo Fisher Scientific).

Superresolution images were obtained using a gSTEDSP8 X (Leica). Samples were imaged at 400 Hz scan speed at unidirectional scanning and detected using gated hybrid SMD GaAsP detectors and a 100× HC PL APO CS2 oil lens with numerical ap-

erture 1.4 (serial no. 506378). Images were acquired at 3× to 5× zoom with a pixel size of 23–24 nm. The fluorophores were excited using a white light laser at 488 and 568 nm. Channels were acquired using a sequential setting starting with the red channel (excitation at 568 nm using a 660-notch filter and emission detection set to 578–634 nm with 0.3–6-ns gating), followed by the green channel (excitation at 488 nm and emission detection of 500–545 nm with gating set to 1.5–7.6 ns) using a 488-notch filter, both using a pinhole of 1 airy unit. The STED laser intensities were at 1.424 for the 592-nm depletion laser (for the green) and 1.323 W for the 660-nm depletion laser (for the red channel). For both channels, frame averaging was set to 3, and line accumulation was set to 2 using a Leica LAS X 3.4.0.18371 software.

Data analysis

Localization analysis of images of GFP–COL–RPE cotransfected with ST-Cherry and antibody labeled against Sec31A (after fixation after live imaging until an accumulation of GFP–COL in the Golgi was visible) was performed automatically. Spatial overlap between Sec31A and GFP–COL was measured using a custom plugin for ImageJ/Fiji (Schindelin et al., 2012; Schneider et al., 2012). First, the punctate Sec31A structures were detected using the Fiji plugin TrackMate (Tinevez et al., 2017), fit with a 2D ellipsoidal Gaussian distribution and false identifications isolated and removed according to a low-pass ellipticity filter. The GFP–COL, visible in a separate imaging channel, exhibited a mixed distribution of punctate and broader objects, which were identified separately then combined. Images were processed before object identification to enhance the respective structures being detected. For punctate GFP–COL structures, images were convolved with a 3D Gaussian kernel to remove noise then processed with a rolling ball filter (Sternberg, 1983) to subtract nonpunctate structures. Punctate GFP–COL structures were subsequently identified using the same approach as for Sec31A but with an additional low-pass sigma (spot width) filter. For broader GFP–COL structures the raw image was also convolved with a 3D Gaussian kernel and rolling-ball filter, albeit with a larger radius. The images were then processed with a 2D median filter and threshholded using the maximum entropy approach (Kapur et al., 1985). Objects were identified as contiguous regions in the binarized image and filtered using a high-pass size filter. At this point, punctate and broad GFP–COL structures were combined, with instances of spatial overlap resolved in favor of broad objects, unless the number of punctate objects per broad object exceeded a user-defined threshold of 5. The GFP–COL also accumulates around the Golgi. To remove these structures from the analysis, Golgi elements are identified in a separate fluorescence channel using a similar approach to the broader GFP–COL structures, except using the isodata thresholding approach (Ridler and Calvard, 1978). Any GFP–COL structures within 0.5 µm of a Golgi are removed. Finally, GFP–COL structures are filtered based on their mean intensity in the GFP–COL channel. Pixel-based overlap of Sec31A and GFP–COL is calculated along with the area of each object projected into the XY plane.

The code for data analysis is included as a ZIP file in Online supplemental material. The plugin and the source code are also publicly accessible on a new GitHub repository (https://github .com/SJCross/ModularImageAnalysis). This is linked to a service called Zenodo, which provides a permanent DOI reference to that specific version (Cross, 2018. The files are as follows: Modular_ Image_Analysis-v0.3.2.jar is the plugin, which now includes all the third-party libraries that were previously stored in the /jars folder; ModularImageAnalysis-v0.3.2.zip is the source code for the plugin itself; Analysis.mia is the MIA workflow file used for the final analysis; Installation and usage.txt describes how to install the plugin and run the Analysis.mia analysis file; LICENSE. txt is the license for the plugin itself; and dependencies.html is an HTML-formatted page listing all the dependencies used by the plugin and their associated licenses. The analysis was performed with n = 4 independent data sets that contained a total of 55 cells.

For estimating diameter sizes of larger GFP-positive objects and small puncta, as well as the closely or colocalizing objects labeling for the inner COPII layer (via Sec24C antibody labeling and mSc-Sec23A in the same channel), whole cells were captured using the confocal mode of the STED, before zooming in on an area of interest (showing colocalization and or bigger GFP-positive structures). Using ImageJ's line tool, a line with a width of 5 pixels for smaller objects, and 10 pixels for larger objects, was drawn through objects of interest and line graphs were generated for both channels. The resulting line graphs were subsequently fitted to one to two Gaussian curves when possible using MAT LAB R2016a (MathWorks), and the FWHM was obtained and calculated to show the FWHM in nanometers. Where multiple peaks existed, the summed FWHM of both fitted Gaussian curves was displayed in the figure instead. For large objects where Gaussian fitting was not possible, the diameters measured manually via ImageJ were selected as estimated diameter. The estimated diameters represent the maximum object diameter of the measured objects. A total of 14 cells were investigated, and 20 objects of interest were measured.

Analysis of protein and RNA abundances

For the GFP trap, Chromotek GFP-Trap_A (GFP-Trap coupled to agarose bead particle size of ∼90 µm; Code gta-20) were used. GFP–COL–RPE and GFP–RPE (used as control) were seeded near confluent on 15-cm dishes and incubated in the presence of ascorbate (50 µg·ml⁻¹) for 24 h, followed by ascorbate starvation for 24 h and by 15-min incubation in presence or absence of 500 µg·ml⁻¹ ascorbate before cell lysis. All following steps were performed at 4°C. The lysis buffer contained 10 mM Tris-HCl (pH 7.4), 50 mM NaCl, 0.5 mM EDTA, 0.5% (vol/vol) IGEPAL and protease inhibitor cocktail (Calbiochem). For cell lysis, cells were rinsed with ice cold PBS and incubated in 0.5 ml lysis buffer for 15 min. Lysates were subsequently collected and incubated for 30 min while gently mixing. Beads were equilibrated with lysis buffer (without protease inhibitor cocktail and IGEPAL; referred to as dilution buffer) using 20 µl of bead slurry per sample. Lysates collected after centrifugation at 13,500 rpm for 10 min were incubated with the GFP-trap beads for 2 h. Samples were subsequently centrifuged at 2,700 g for 2 min to collect the beads with bound sample. After they were washed twice with dilution buffer containing protease inhibitor cocktail, samples were boiled after addition of 43 µl 2× LDS buffer containing a reducing agent (Invitrogen) at 95°C for 10 min, and beads were separated from the

McCaughey et al.
ER-to-Golgi traffic of procollagen

Journal of Cell Biology
https://doi.org/10.1083/jcb.201806035

944

denatured protein samples by centrifugation as described above. The entire sample was loaded onto a 3–8% Tris-Acetate precast gel (NuPAGE) and run for 135 min at 100 V in Tris-Acetate running buffer supplemented with antioxidant (all Invitrogen).

Gel slices were subsequently cut and digested for proteomics analysis via mass spectrometry. Each gel lane was cut into six slices, and each slice was subjected to reduction (10 mM DTT, 56°C for 30 min), alkylation (55 mM iodoacetamide, RT for 20 min), and in-gel tryptic digestion (1.25 µg trypsin per gel slice, 37°C overnight). The resulting peptides were fractionated using an Ultimate 3000 nano-LC system in line with an LTQ-Orbitrap Velos mass spectrometer (Thermo Fisher Scientific). In brief, peptides in 1% (vol/vol) formic acid were injected onto an Ac-claim PepMap C18 nanotrap column (Thermo Fisher Scientific). After washing with 0.5% (vol/vol) acetonitrile 0.1% (vol/vol) formic acid peptides were resolved on a 250 mm × 75 µm Acclaim PepMap C18 reverse phase analytical column (Thermo Fisher Scientific) over a 150-min organic gradient, using seven gradient segments (1–6% solvent B over 1 min, 6–15% B over 58 min, 15–32% B over 58 min, 32–40% B over 5 min, 40–90% B over 1 min, held at 90% B for 6 min, and then reduced to 1% B over 1 min) with a flow rate of 300 nl·min^{-1}. Solvent A was 0.1% formic acid, and solvent B was aqueous 80% acetonitrile in 0.1% formic acid. Peptides were ionized by nanoelectrospray ionization at 2.1 kV using a stainless-steel emitter with an internal diameter of 30 µm (Thermo Fisher Scientific) and a capillary temperature of 250°C. Tandem mass spectra were acquired using an LTQ-Orbitrap Velos mass spectrometer controlled by Xcalibur 2.1 software (Thermo Fisher Scientific) and operated in data-dependent acquisition mode. The Orbitrap was set to analyze the survey scans at 60,000 resolution (at mass to charge ratio [m/z] 400) in the mass range m/z 300–2,000 and the top 20 multiply charged ions in each duty cycle selected for tandem mass spectrometry in the LTQ linear ion trap. Charge state filtering, where unassigned precursor ions were not selected for fragmentation, and dynamic exclusion (repeat count, 1; repeat duration, 30 s; exclusion list size, 500) were used. Fragmentation conditions in the LTQ were as follows: normalized collision energy, 40%; activation q, 0.25; activation time, 10 ms; and minimum ion selection intensity, 500 counts.

The raw data files were processed and quantified using Proteome Discoverer software v1.4 (Thermo Fisher Scientific) and searched against the UniProt Human database (downloaded September 14, 2017; 140,000 sequences) plus the GFP sequence using the SEQUEST algorithm. Peptide precursor mass tolerance was set at 10 ppm, and tandem mass spectrometry tolerance was set at 0.8 D. Search criteria included carbamidomethylation of cysteine (+57.0214) as a fixed modification and oxidation of methionine and proline (+15.9949) as variable modifications. Searches were performed with full tryptic digestion, and a maximum of three missed cleavage sites were allowed. The reverse database search option was enabled, and all peptide data were filtered to satisfy false-discovery rate of 1%.

The RNA-seq data from WT RPE-1 cells was derived from our own previously published data (Stevenson et al., 2017). Raw RNA-seq data are available in the ArrayExpress database under accession no. E-MTAB-5618.

For semiquantitative analysis of protein levels of Sec24A and Sec24C and COL1a1 levels in WT RPE-1, GFP–RPE, and GFP–COL–RPE cells, cells were seeded on 10-cm dishes and grown for 4 d. Cells were incubated in 2 ml serum-free culture medium supplemented with (Sec24C and D lysates, as well as COL1A1) or without 50 µg·ml^{-1} ascorbic acid for 24 h. The medium was collected, and the cells were lysed for 15 min in buffer containing 50 mM Tris-HCl, 150 mM NaCl, 1% (vol/vol) Triton X-100, and 1% (vol/vol) protease inhibitor cocktail (Calbiochem) at pH 7.4 on ice. Protein fractions of medium and lysate were centrifuged at 13,500 rpm at 4°C for 10 min. The cell pellet was discarded. The supernatant was denatured and run under reducing conditions on a 3–8% Tris-Acetate precast gel (NuPAGE) for 135 min at 100 V in Tris-Acetate running buffer supplemented with antioxidant. Transfer of protein bands onto a nitrocellulose membrane was performed at 15 V overnight. The membrane was blocked using 5% (wt/vol) milk powder in TBST for 30 min at RT and incubated with antibodies against COL1A1 (Novus Biologicals; 0.5 µg·ml^{-1}), Sec24A (Satchwell et al., 2013), and Sec24C (1:100) and 0.5 µg·ml^{-1} mouse monoclonal anti-GAPDH (AM4300; Thermo Fisher Scientific) as loading control for 1.5 h at RT. After repeated rinsing with TBS-Tween, the membrane was incubated for 1.5 h at RT with HRP-conjugated antibodies diluted in the blocking solution (1:5,000) against mouse and rabbit, respectively (Jackson ImmunoResearch). The wash step was repeated, and detection was performed using Promega WB-ECL reaction reagents and autoradiography films with overnight exposure and subsequent development. Cells from the Sec31A, Sec12, and TFG blots were incubated in normal culture medium before cell lysis and scraping. The immunoblot for Sec31A was done as described above, while Western blots showing intracellular levels of Sec12 (a gift from Balch laboratory, Scripps Research Institute, La Jolla, CA; Weissman et al., 2001) and TFG (0.05 µg·ml^{-1}, NBP2-24485; Novus Biologicals) were run on a 4–12% Bis-Tris (NuPAGE) precast gel at 200 V in MOPS running buffer for 50 min instead.

Online supplemental material

Fig. S1 shows that GFP–COL transport is ascorbate and biotin controllable. Fig. S2 shows that transport of GFP–COL to the Golgi occurs without the use of large carriers. Fig. S3 shows that large GFP–COL structures are not positive for autophagosomal or endosomal markers. Fig. S4 shows that labeling of collagen type I in fibroblasts using various antibodies shows no apparent large structures. Fig. S5 shows NZ efficacy and collagen and COPII levels in RPE. Video 1 shows ascorbate- and biotin-dependent trafficking of GFP–COL. Video 2 shows that transport of GFP–COL to the Golgi using the RUSH system is biotin controllable. Video 3 shows that transport of GFP–COL to the Golgi is not cell type specific. Video 4 shows transport of GFP–COL to the Golgi in IMR-90 human lung fibroblasts. Video 5 shows that transport of GFP–COL to the Golgi occurs without the use of large carriers. Videos 6 and 7 show GFP–COL transport to the Golgi in RPE-1 cells. Video 8 shows GFP–COL transport from the ER to the Golgi, before fixation and colabeling with antibodies of interest. Video 9 shows that transport of GFP–COL to the Golgi is COPII dependent. Video 10 shows that GFP–COL transport to the Golgi is independent of microtubules.

McCaughey et al.
ER-to-Golgi traffic of procollagen

Journal of Cell Biology
https://doi.org/10.1083/jcb.201806035

945

Submitted: 5 June 2018
Revised: 17 October 2018
Accepted: 6 December 2018

References

Aridor, M., S.I. Bannykh, T. Rowe, and W.E. Balch. 1995. Sequential coupling between COPII and COPI vesicle coats in endoplasmic reticulum to Golgi transport. *J. Cell Biol.* 131:875–893. https://doi.org/10.1083/jcb.131.4.875

Asante, D., N.L. Stevenson, and D.J. Stephens. 2014. Subunit composition of the human cytoplasmic dynein-2 complex. *J. Cell Sci.* 127:4774–4787. https://doi.org/10.1242/jcs.159038

Bächinger, H.P., K.J. Doege, J.P. Petschek, L.I. Fessler, and J.H. Fessler. 1982. Structural implications from an electronmicroscopic comparison of procollagen V with procollagen I, pC-collagen I, procollagen IV, and a Drosophila procollagen. *J. Biol. Chem.* 257:14590–14592.

Betin, V.M., B.K. Singleton, S.F. Parsons, D.J. Anstee, and J.D. Lane. 2013. Autophagy facilitates organelle clearance during differentiation of human erythroblasts: Evidence for a role for ATG4 paralogs during autophagosome maturation. *Autophagy.* 9:881–893. https://doi.org/10.4161/auto.24172

Bindels, D.S., L. Haarbosch, L. van Weeren, M. Postma, K.E. Wiese, M. Mastop, S. Aumonier, G. Gotthard, A. Royant, M.A. Hink, and T.W. Gadella Jr. 2017. mScarlet: A bright monomeric red fluorescent protein for cellular imaging. *Nat. Methods.* 14:53–56. https://doi.org/10.1038/nmeth.4074

Blanck, T.J., and B. Peterkofsky. 1975. The stimulation of collagen secretion by ascorbate as a result of increased proline hydroxylation in chick embryo fibroblasts. *Arch. Biochem. Biophys.* 171:259–267. https://doi.org/10.1016/0003-9861(75)90031-4

Boncompain, G., S. Divoux, N. Gareil, H. de Forges, A. Lescure, L. Latreche, V. Mercanti, F. Jollivet, G. Raposo, and F. Perez. 2012. Synchronization of secretory protein traffic in populations of cells. *Nat. Methods.* 9:493–498. https://doi.org/10.1038/nmeth.1928

Bonfanti, L., A.A. Mironov Jr., J.A. Martínez-Menárguez, O. Martella, A. Fusella, M. Baldassarre, R. Buccione, H.J. Geuze, A.A. Mironov, and A. Luini. 1998. Procollagen traverses the Golgi stack without leaving the lumen of cisternae: Evidence for cisternal maturation. *Cell.* 95:993–1003. https://doi.org/10.1016/S0092-8674(00)81723-7

Bourhis, J.M., N. Mariano, Y. Zhao, K. Harlos, J.Y. Exposito, E.Y. Jones, C. Moali, N. Aghajari, and D.J. Hulmes. 2012. Structural basis of fibrillar collagen trimerization and related genetic disorders. *Nat. Struct. Mol. Biol.* 19:1031–1036. https://doi.org/10.1038/nsmb.2389

Boyadjiev, S.A., J.C. Fromme, J. Ben, S.S. Chong, C. Nauta, D.J. Hur, G. Zhang, S. Hamamoto, R. Schekman, M. Ravazzola, et al. 2006. Cranio-lenticulo-sutural dysplasia is caused by a SEC23A mutation leading to abnormal endoplasmic-reticulum-to-Golgi trafficking. *Nat. Genet.* 38:1192–1197. https://doi.org/10.1038/ng1876

Cabral, W.A., E. Makareeva, A. Colige, A.D. Letocha, J.M. Ty, H.N. Yeowell, G. Pals, S. Leikin, and J.C. Marini. 2005. Mutations near amino end of alpha1(I) collagen cause combined osteogenesis imperfecta/Ehlers-Danlos syndrome by interference with N-propeptide processing. *J. Biol. Chem.* 280:19259–19269. https://doi.org/10.1074/jbc.M414698200

Canty, E.G., and K.E. Kadler. 2005. Procollagen trafficking, processing and fibrillogenesis. *J. Cell Sci.* 118:1341–1353. https://doi.org/10.1242/jcs.01731

Costantini, L.M., M. Fossati, M. Francolini, and E.L. Snapp. 2012. Assessing the tendency of fluorescent proteins to oligomerize under physiologic conditions. *Traffic.* 13:643–649. https://doi.org/10.1111/j.1600-0854.2012.01336.x

Cross, S.2018. SJCross/ModularImageAnalysis: Version 0.5.6. (accessed May 24, 2018). https://doi.org/10.5281/zenodo.1252337

Duran, I., L. Nevarez, A. Sarukhanov, S. Wu, K. Lee, P. Krejci, M. Weis, D. Eyre, D. Krakow, and D.H. Cohn. 2015. HSP47 and FKBP65 cooperate in the synthesis of type I procollagen. *Hum. Mol. Genet.* 24:1918–1928. https://doi.org/10.1093/hmg/ddu608

Fisher, L.W., J.T. Stubbs III, and M.F. Young. 1995. Antisera and cDNA probes to human and certain animal model bone matrix noncollagenous proteins. *Acta Orthop. Scand. Suppl.* 266:61–65. https://doi.org/10.3109/17453679509157649

Forlino, A., and J.C. Marini. 2016. Osteogenesis imperfecta. *Lancet.* 387:1657–1671. https://doi.org/10.1016/S0140-6736(15)00728-X

Fourriere, L., S. Divoux, M. Roceri, F. Perez, and G. Boncompain. 2016. Microtubule-independent secretion requires functional maturation of Golgi elements. *J. Cell Sci.* 129:3238–3250. https://doi.org/10.1242/jcs.188870

Garbes, L., K. Kim, A. Rieß, H. Hoyer-Kuhn, A. Beleggia, A. Bevot, M.J. Kim, Y.H. Huh, H.S. Kweon, R. Savarirayan, et al. 2015. Mutations in SEC24D, encoding a component of the COPII machinery, cause a syndromic form of osteogenesis imperfecta. *Am. J. Hum. Genet.* 96:432–439. https://doi.org/10.1016/j.ajhg.2015.01.002

Goldberg, B., E.H. Epstein Jr., and C.J. Sherr. 1972. Precursors of collagen secreted by cultured human fibroblasts. *Proc. Natl. Acad. Sci. USA.* 69:3655–3659. https://doi.org/10.1073/pnas.69.12.3655

Gorur, A., L. Yuan, S.J. Kenny, S. Baba, K. Xu, and R. Schekman. 2017. COPII-coated membranes function as transport carriers of intracellular procollagen I. *J. Cell Biol.* 216:1745–1759. https://doi.org/10.1083/jcb.201702135

Hughes, H., and D.J. Stephens. 2010. Sec16A defines the site for vesicle budding from the endoplasmic reticulum on exit from mitosis. *J. Cell Sci.* 123:4032–4038. https://doi.org/10.1242/jcs.076000

Ishikawa, Y., S. Ito, K. Nagata, L.Y. Sakai, and H.P. Bächinger. 2016. Intracellular mechanisms of molecular recognition and sorting for transport of large extracellular matrix molecules. *Proc. Natl. Acad. Sci. USA.* 113:E6036–E6044. https://doi.org/10.1073/pnas.1609571113

Ito, S., and K. Nagata. 2017. Biology of Hsp47 (Serpin H1), a collagen-specific molecular chaperone. *Semin. Cell Dev. Biol.* 62:142–151. https://doi.org/10.1016/j.semcdb.2016.11.005

Jimenez, S., M. Harsch, and J. Rosenbloom. 1973. Hydroxyproline stabilizes the triple helix of chick tendon collagen. *Biochem. Biophys. Res. Commun.* 52:106–114. https://doi.org/10.1016/0006-291X(73)90960-1

Jimenez, S.A., R.I. Bashey, M. Benditt, and R. Yankowski. 1977. Identification of collagen alpha1(I) trimer in embryonic chick tendons and calvaria. *Biochem. Biophys. Res. Commun.* 78:1354–1361. https://doi.org/10.1016/0006-291X(77)91441-3

Jin, L., K.B. Pahuja, K.E. Wickliffe, A. Gorur, C. Baumgärtel, R. Schekman, and M. Rape. 2012. Ubiquitin-dependent regulation of COPII coat size and function. *Nature.* 482:495–500. https://doi.org/10.1038/nature10822

Jobling, R., R. D'Souza, N. Baker, I. Lara-Corrales, R. Mendoza-Londono, L. Dupuis, R. Savarirayan, L. Ala-Kokko, and P. Kannu. 2014. The collagenopathies: Review of clinical phenotypes and molecular correlations. *Curr. Rheumatol. Rep.* 16:394. https://doi.org/10.1007/s11926-013-0394-3

Kadler, K.E., Y. Hojima, and D.J. Prockop. 1990. Collagen fibrils in vitro grow from pointed tips in the C- to N-terminal direction. *Biochem. J.* 268:339–343. https://doi.org/10.1042/bj2680339

Kano, F., H. Kondo, A. Yamamoto, A.R. Tanaka, N. Hosokawa, K. Nagata, and M. Murata. 2005. The maintenance of the endoplasmic reticulum network is regulated by p47, a cofactor of p97, through phosphorylation by cdc2 kinase. *Genes Cells.* 10:333–344. https://doi.org/10.1111/j.1365-2443.2005.00837.x

Kapur, J.N., P.K. Sahoo, and A.K.C. Wong. 1985. A new method for gray-level picture thresholding using the entropy of the histogram. *Comput. Vis. Graph. Image Process.* 29:273–285. https://doi.org/10.1016/0734-189X(85)90125-2

Koide, T., S. Asada, Y. Takahara, Y. Nishikawa, K. Nagata, and K. Kitagawa. 2006. Specific recognition of the collagen triple helix by chaperone HSP47: Minimal structural requirement and spatial molecular orientation. *J. Biol. Chem.* 281:3432–3438. https://doi.org/10.1074/jbc.M509707200

Kurokawa, K., M. Okamoto, and A. Nakano. 2014. Contact of cis-Golgi with ER exit sites executes cargo capture and delivery from the ER. *Nat. Commun.* 5:3653. https://doi.org/10.1038/ncomms4653

Lang, M.R., L.A. Lapierre, M. Frotscher, J.R. Goldenring, and E.W. Knapik. 2006. Secretory COPII coat component Sec23a is essential for craniofacial chondrocyte maturation. *Nat. Genet.* 38:1198–1203. https://doi.org/10.1038/ng1880

Lightfoot, S.J., D.F. Holmes, A. Brass, M.E. Grant, P.H. Byers, and K.E. Kadler. 1992. Type I procollagens containing substitutions of aspartate, arginine, and cysteine for glycine in the pro alpha 1 (I) chain are cleaved slowly by N-proteinase, but only the cysteine substitution introduces a kink in the molecule. *J. Biol. Chem.* 267:25521–25528.

Lu, Y., S.A. Kamel-El Sayed, K. Wang, L.M. Tiede-Lewis, M.A. Grillo, P.A. Veno, V. Dusevich, C.L. Phillips, L.F. Bonewald, and S.L. Dallas. 2018. Live imaging of type I collagen assembly dynamics in osteoblasts stably expressing GFP and mCherry-tagged collagen constructs. *J. Bone Miner. Res.* 33:1166–1182. https://doi.org/10.1002/jbmr.3409

Ma, W., and J. Goldberg. 2016. TANGO1/cTAGE5 receptor as a polyvalent template for assembly of large COPII coats. *Proc. Natl. Acad. Sci. USA.* 113:10061–10066. https://doi.org/10.1073/pnas.1605916113

Malfait, F., S. Symoens, N. Goemans, Y. Gyftodimou, E. Holmberg, V. López-González, G. Mortier, S. Nampoothiri, M.B. Petersen, and A. De Paepe. 2013. Helical mutations in type I collagen that affect the processing of the amino-propeptide result in an Osteogenesis Imperfecta/Ehlers-Danlos Syndrome overlap syndrome. *Orphanet J. Rare Dis.* 8:78. https://doi.org/10.1186/1750-1172-8-78

Malhotra, V., and P. Erlmann. 2015. The pathway of collagen secretion. *Annu. Rev. Cell Dev. Biol.* 31:109–124. https://doi.org/10.1146/annurev-cellbio-100913-013002

Malhotra, V., P. Erlmann, and C. Nogueira. 2015. Procollagen export from the endoplasmic reticulum. *Biochem. Soc. Trans.* 43:104–107. https://doi.org/10.1042/BST20140286

McCaughey, J., V.J. Miller, N.L. Stevenson, A.K. Brown, A. Budnik, K.J. Heesom, D. Alibhai, and D.J. Stephens. 2016. TFG promotes organization of transitional ER and efficient collagen secretion. *Cell Reports.* 15:1648–1659. https://doi.org/10.1016/j.celrep.2016.04.062

McGourty, C.A., D. Akopian, C. Walsh, A. Gorur, A. Werner, R. Schekman, D. Bautista, and M. Rape. 2016. Regulation of the CUL3 ubiquitin ligase by a calcium-dependent co-adaptor. *Cell.* 167:525–538.e14. https://doi.org/10.1016/j.cell.2016.09.026

Miller, E.A., and R. Schekman. 2013. COPII—A flexible vesicle formation system. *Curr. Opin. Cell Biol.* 25:420–427. https://doi.org/10.1016/j.ceb.2013.04.005

Moosa, S., B.H. Chung, J.Y. Tung, J. Altmuller, H. Thiele, P. Nurnberg, C. Netzer, G. Nishimura, and B. Wollnik. 2016. Mutations in SEC24D cause autosomal recessive osteogenesis imperfecta. *Clin. Genet.* 89:517–519. https://doi.org/10.1111/cge.12678

Mussini, E., J.J. Hutton Jr., and S. Udenfriend. 1967. Collagen proline hydroxylase in wound healing, granuloma formation, scurvy, and growth. *Science.* 157:927–929. https://doi.org/10.1126/science.157.3791.927

Nogueira, C., P. Erlmann, J. Villeneuve, A.J. Santos, E. Martínez-Alonso, J.A. Martínez-Menárguez, and V. Malhotra. 2014. SLY1 and Syntaxin 18 specify a distinct pathway for procollagen VII export from the endoplasmic reticulum. *eLife.* 3:e02784. https://doi.org/10.7554/eLife.02784

Oecal, S., E. Socher, M. Uthoff, C. Ernst, F. Zaucke, H. Sticht, U. Baumann, and J.M. Gebauer. 2016. The pH-dependent client release from the collagen-specific chaperone HSP47 is triggered by a tandem histidine pair. *J. Biol. Chem.* 291:12612–12626. https://doi.org/10.1074/jbc.M115.706069

Ono, T., T. Miyazaki, Y. Ishida, M. Uehata, and K. Nagata. 2012. Direct in vitro and in vivo evidence for interaction between Hsp47 protein and collagen triple helix. *J. Biol. Chem.* 287:6810–6818. https://doi.org/10.1074/jbc.M111.280248

Palmer, K.J., J.E. Konkel, and D.J. Stephens. 2005. PCTAIRE protein kinases interact directly with the COPII complex and modulate secretory cargo transport. *J. Cell Sci.* 118:3839–3847. https://doi.org/10.1242/jcs.02496

Pickard, A., A. Adamson, Y. Lu, J. Chang, R. Garva, N. Hodson, and K. Kadler. 2018. Collagen assembly and turnover imaged with a CRISPR-Cas9 engineered Dendra2 tag. *bioRxiv.* (Preprint posted June 5, 2018). https://doi.org/10.1101/331496

Raote, I., M. Ortega Bellido, M. Pirozzi, C. Zhang, D. Melville, S. Parashuraman, T. Zimmermann, and V. Malhotra. 2017. TANGO1 assembles into rings around COPII coats at ER exit sites. *J. Cell Biol.* 216:901–909. https://doi.org/10.1083/jcb.201608080

Raote, I., M. Ortega-Bellido, A.J. Santos, O. Foresti, C. Zhang, M.F. Garcia-Parajo, F. Campelo, and V. Malhotra. 2018. TANGO1 builds a machine for collagen export by recruiting and spatially organizing COPII, tethers and membranes. *eLife.* 7:e32723. https://doi.org/10.7554/eLife.32723

Rezaei, N., A. Lyons, and N.R. Forde. 2018. Environmentally controlled curvature of single collagen proteins. *Biophys. J.* 115:1457–1469. https://doi.org/10.1016/j.bpj.2018.09.003

Ridler, T.W., and S. Calvard. 1978. Picture thresholding using an iterative selection method. *IEEE Trans. Syst. Man Cybern.* 8:630–632. https://doi.org/10.1109/TSMC.1978.4310039

Saito, K., and T. Katada. 2015. Mechanisms for exporting large-sized cargoes from the endoplasmic reticulum. *Cell. Mol. Life Sci.* 72:3709–3720. https://doi.org/10.1007/s00018-015-1952-9

Saito, K., M. Chen, F. Bard, S. Chen, H. Zhou, D. Woodley, R. Polischuk, R. Schekman, and V. Malhotra. 2009. TANGO1 facilitates cargo loading at endoplasmic reticulum exit sites. *Cell.* 136:891–902. https://doi.org/10.1016/j.cell.2008.12.025

Saito, K., K. Yamashiro, Y. Ichikawa, P. Erlmann, K. Kontani, V. Malhotra, and T. Katada. 2011. cTAGE5 mediates collagen secretion through interaction with TANGO1 at endoplasmic reticulum exit sites. *Mol. Biol. Cell.* 22:2301–2308. https://doi.org/10.1091/mbc.e11-02-0143

Salo, V.T., I. Belevich, S. Li, L. Karhinen, H. Vihinen, C. Vigouroux, J. Magré, C. Thiele, M. Hölttä-Vuori, E. Jokitalo, and E. Ikonen. 2016. Seipin regulates ER-lipid droplet contacts and cargo delivery. *EMBO J.* 35:2699–2716. https://doi.org/10.15252/embj.201695170

Santos, A.J., I. Raote, M. Scarpa, N. Brouwers, and V. Malhotra. 2015. TANGO1 recruits ERGIC membranes to the endoplasmic reticulum for procollagen export. *eLife.* 4:e10982. https://doi.org/10.7554/eLife.10982

Sarmah, S., A. Barrallo-Gimeno, D.B. Melville, J. Topczewski, L. Solnica-Krezel, and E.W. Knapik. 2010. Sec24D-dependent transport of extracellular matrix proteins is required for zebrafish skeletal morphogenesis. *PLoS One.* 5:e10367. https://doi.org/10.1371/journal.pone.0010367

Satchwell, T.J., S. Pellegrin, P. Bianchi, B.R. Hawley, A. Gampel, K.E. Mordue, A. Budnik, E. Fermo, W. Barcellini, D.J. Stephens, et al. 2013. Characteristic phenotypes associated with congenital dyserythropoietic anemia (type II) manifest at different stages of erythropoiesis. *Haematologica.* 98:1788–1796. https://doi.org/10.3324/haematol.2013.085522

Satoh, M., K. Hirayoshi, S. Yokota, N. Hosokawa, and K. Nagata. 1996. Intracellular interaction of collagen-specific stress protein HSP47 with newly synthesized procollagen. *J. Cell Biol.* 133:469–483. https://doi.org/10.1083/jcb.133.2.469

Schindelin, J., I. Arganda-Carreras, E. Frise, V. Kaynig, M. Longair, T. Pietzsch, S. Preibisch, C. Rueden, S. Saalfeld, B. Schmid, et al. 2012. Fiji: an open-source platform for biological-image analysis. *Nat. Methods.* 9:676–682. https://doi.org/10.1038/nmeth.2019

Schmidt, K., F. Cavodeassi, Y. Feng, and D.J. Stephens. 2013. Early stages of retinal development depend on Sec13 function. *Biol. Open.* 2:256–266. https://doi.org/10.1242/bio.20133251

Schneider, C.A., W.S. Rasband, and K.W. Eliceiri. 2012. NIH Image to ImageJ: 25 years of image analysis. *Nat. Methods.* 9:671–675. https://doi.org/10.1038/nmeth.2089

Stephens, D.J. 2012. Cell biology: Collagen secretion explained. *Nature.* 482:474–475. https://doi.org/10.1038/482474a

Stephens, D.J., and R. Pepperkok. 2002. Imaging of procollagen transport reveals COPI-dependent cargo sorting during ER-to-Golgi transport in mammalian cells. *J. Cell Sci.* 115:1149–1160.

Sternberg, S.R. 1983. Biomedical image processing. *Computer.* 16:22–34. https://doi.org/10.1109/MC.1983.1654163

Stevenson, N.L., D.J.M. Bergen, R.E.H. Skinner, E. Kague, E. Martin-Silverstone, K.A. Robson Brown, C.L. Hammond, and D.J. Stephens. 2017. Giantin-knockout models reveal a feedback loop between Golgi function and glycosyltransferase expression. *J. Cell Sci.* 130:4132–4143. https://doi.org/10.1242/jcs.212308

Tasab, M., M.R. Batten, and N.J. Bulleid. 2000. Hsp47: A molecular chaperone that interacts with and stabilizes correctly-folded procollagen. *EMBO J.* 19:2204–2211. https://doi.org/10.1093/emboj/19.10.2204

Tasab, M., L. Jenkinson, and N.J. Bulleid. 2002. Sequence-specific recognition of collagen triple helices by the collagen-specific molecular chaperone HSP47. *J. Biol. Chem.* 277:35007–35012. https://doi.org/10.1074/jbc.M202782200

Tinevez, J.Y., N. Perry, J. Schindelin, G.M. Hoopes, G.D. Reynolds, E. Laplantine, S.Y. Bednarek, S.L. Shorte, and K.W. Eliceiri. 2017. TrackMate: An open and extensible platform for single-particle tracking. *Methods.* 115:80–90. https://doi.org/10.1016/j.ymeth.2016.09.016

Townley, A.K., Y. Feng, K. Schmidt, D.A. Carter, R. Porter, P. Verkade, and D.J. Stephens. 2008. Efficient coupling of Sec23-Sec24 to Sec13-Sec31 drives COPII-dependent collagen secretion and is essential for normal craniofacial development. *J. Cell Sci.* 121:3025–3034. https://doi.org/10.1242/jcs.031070

Townley, A.K., K. Schmidt, L. Hodgson, and D.J. Stephens. 2012. Epithelial organization and cyst lumen expansion require efficient Sec13-Sec31-driven secretion. *J. Cell Sci.* 125:673–684. https://doi.org/10.1242/jcs.091355

Uitto, J. 1979. Collagen polymorphism: Isolation and partial characterization of alpha 1(I)-trimer molecules in normal human skin. *Arch. Biochem. Biophys.* 192:371–379. https://doi.org/10.1016/0003-9861(79)90105-X

Venditti, R., T. Scanu, M. Santoro, G. Di Tullio, A. Spaar, R. Gaibisso, G.V. Beznoussenko, A.A. Mironov, A. Mironov Jr., L. Zelante, et al. 2012. Sedlin controls the ER export of procollagen by regulating the Sar1 cycle. *Science.* 337:1668–1672. https://doi.org/10.1126/science.1224947

Venditti, R., C. Wilson, and M.A. De Matteis. 2014. Exiting the ER: What we know and what we don't. *Trends Cell Biol.* 24:9–18. https://doi.org/10.1016/j.tcb.2013.08.005

Weissman, J.T., H. Plutner, and W.E. Balch. 2001. The mammalian guanine nucleotide exchange factor mSec12 is essential for activation of the Sar1 GTPase directing endoplasmic reticulum export. *Traffic.* 2:465–475. https://doi.org/10.1034/j.1600-0854.2001.20704.x

Yuan, L., S. Baba, K. Bajaj, and R. Schekman. 2017. Cell-free generation of COPII-coated procollagen I carriers. *Bio Protoc.* 7:e2450. https://doi.org/10.21769/BioProtoc.2450